Evaluating the On-Sky Sensitivity of DESHIMA 2.0

Chasing the Photon-Noise Limit in Submillimetre Astronomy

Madelief Peters

Delft University of Technology

TU Delft

Evaluating the On-Sky Sensitivity of DESHIMA 2.0

Chasing the Photon-Noise Limit in Submillimetre Astronomy

by

Madelief Peters

To obtain the degree of Bachelor of Science in Applied Physics
at the Delft University of Technology

Student number:	5504635
Supervisor:	A. Endo
Examiner:	S. Otte
Project Duration:	September 2, 2024 – December 13, 2024
Study Programme:	Bachelor of Applied Physics
Faculty:	Faculty of Applied Sciences
Cover:	A photograph of the Atacama Desert in Chile, *taken by the author from the peak of Llano de Chajnantor*

TU Delft

Abstract

The DESHIMA 2.0 spectrometer, installed on the ASTE telescope, is designed to enable broadband, high-sensitivity observations in the submillimetre wavelength range. This design allows simultaneous observation across a wide frequency range, making it possible to detect multiple emission lines in a single measurement. This is particularly useful for identifying emission lines from distant galaxies with unknown redshifts, allowing redshift determination in a single observation. This study evaluates the sensitivity and noise limitations of DESHIMA 2.0, addressing whether its on-sky performance aligns with a photon-noise model and lab-measured instrument characteristics.

First, the sensitivity of DESHIMA 2.0, integrated with the ASTE telescope, is assessed under fixed telescope conditions by observing the atmospheric signal without nodding the telescope or beam-switching. Observations confirm that the instrument operates near the photon-noise limit, consistent with theoretical predictions and laboratory measurements.

Next, a combined ABBA chopping-and-nodding technique, which integrates beam-switching with nodding of the telescope, is implemented to mitigate atmospheric noise during observations. This study demonstrates that this approach effectively filters out atmospheric noise over integration times of up to 3000 seconds, achieving a standard deviation of the noise level on the order of 10^{-4} K in the 250 to 300 GHz range. These findings confirm that the instrument maintains photon-noise-limited performance under varying atmospheric conditions.

Finally, the observed spectrum of Mars is compared to its known spectral characteristics to validate the sensitivity and calibration of DESHIMA 2.0 for bright astronomical sources. Although the observed spectrum closely resembles the known spectrum of Mars, the remaining channel-to-channel deviations exceed what the photon-noise model predicts. This highlights the presence of systematic calibration errors and deviations in noise behaviour. These results underscore the need for further refinement of the calibration process and the ABBA chopping analysis to enhance performance for fainter astronomical sources.

Overall, this study establishes that DESHIMA 2.0 achieves photon-noise-limited performance under specific observational setups, marking an important milestone for high-sensitivity submillimetre astronomy. However, further work is needed to optimize the system for detecting weaker signals from distant sources, such as dusty star-forming galaxies, where signal strengths are much weaker.

Contents

1

Introduction

Submillimetre astronomy plays a crucial role in advancing our understanding of the universe, particularly by discovering cold astrophysical objects like dusty star-forming galaxies (DSFGs). These galaxies are among the most luminous in the cosmos, with intense star formation rates of 100–1000 solar masses per year, significantly contributing to the cosmic star formation density at high redshifts [25][15]. DSFGs are hidden in dust that absorbs ultraviolet and optical light, re-emitting it in the infrared and submillimetre wavelengths, making them invisible to optical telescopes and requiring submillimetre observations to detect them [15][10]. Studying DSFGs sheds light on early galaxy evolution, offering insights into the rapid build-up of stellar mass and the formation of massive elliptical galaxies [15][5]. However, such observations face significant challenges due to atmospheric noise, which affect the sensitivity of submillimetre instruments [25]. To accurately detect faint signals and enable reliable studies of DSFGs under real observing conditions, achieving photon-noise-limited sensitivity is essential [25][10].

Figure 1.1: DESHIMA 2.0 at the Atacama Submillimetre Telescope Experiment (ASTE).

To tackle these challenges, particularly the astronomical challenge of determining the redshift of DSFGs, which requires a wide instantaneous bandwidth, the DESHIMA 2.0 spectrometer has been developed and installed on the Atacama Submillimetre Telescope Experiment (ASTE). DESHIMA addresses this challenge by employing an integrated superconducting spectrometer (ISS) with ultra-wideband coverage, enabling the detection of multiple spectral lines within a single observation. This wideband

capability is crucial for accurate redshift measurements of faint objects like DSFGs [10]. Additionally, DESHIMA is designed to operate at photon-noise-limited sensitivity, which is necessary for reducing the impact of atmospheric noise and ensuring reliable detection of faint signals under real observing conditions [10]. Its predecessor, DESHIMA 1.0, demonstrated the feasibility of this concept by successfully detecting a nearby luminous infrared galaxy (LIRG) using a similar spectrometer design [10] [2].

This report builds on that foundation by evaluating DESHIMA 2.0's on-sky sensitivity, validating its photon-noise-limited performance, and improving noise filtering techniques. These efforts aim to establish DESHIMA 2.0 as a powerful tool for submillimetre astronomy, paving the way for ground-breaking discoveries about the history of the universe and enabling the system to fulfil its full potential in this field.

This study aims to evaluate the on-sky performance of DESHIMA 2.0 in terms of sensitivity and noise limitations, addressing whether it operates at the photon-noise limit predicted by theoretical and lab-based models. To address this, the following research question is formulated:

> *"Is the sensitivity of DESHIMA 2.0 on the ASTE telescope (measured on-sky) consistent with a photon-noise model and lab-measured instrument characteristics?"*

To be able to address this, three subquestions are formulated:

1. How does the sensitivity of DESHIMA 2.0 on the ASTE telescope, when observing the atmosphere without moving the telescope, compare to the photon-noise limit predicted by an analytical model based on lab-measured instrument characteristics?
2. How can ABBA chopping be used and refined to make it more effective in removing atmospheric noise and systematic effects?
3. Does the observed spectrum of Mars with DESHIMA 2.0 align with the known spectral characteristics of Mars, verifying the telescope's sensitivity and calibration?

By answering these questions, we aim to (1) establish the fundamental performance of the telescope in atmospheric observations, (2) study the effectiveness of the ABBA chopping method for removing noise and systematic effects, and (3) apply the resulting sensitivity insights to verify DESHIMA's accuracy with a known astronomical source.

To address these objectives, the study combines analytical modelling, noise filtering techniques, and observational validation. First, we test DESHIMA's sensitivity against photon-noise predictions by observing just the atmosphere. Next, we refine the ABBA chopping technique, a method for countering atmospheric noise, to optimise its performance during observations [24]. Finally, we validate the instrument's spectral sensitivity and calibration by comparing the observed spectrum of Mars to its known characteristics. These methods collectively assess DESHIMA 2.0's ability to deliver photon-noise-limited performance.

Establishing photon-noise-limited performance for DESHIMA 2.0 is a vital step toward enabling high-sensitivity submillimetre observations of faint, distant objects, such as DSFGs. This study's findings will contribute to advancing submillimetre astronomy by validating a new generation of instruments capable of addressing the technical challenges of observing the universe's most obscured regions. In the future, this work will support large-scale spectroscopic surveys and detailed studies of high-redshift galaxies, facilitating deeper insights into the early universe.

2

DESHIMA 2.0: System Overview and Theory

2.1. System Overview

DESHIMA 2.0 is a spectrometer system designed for submillimetre-wave observations. It is an upgraded version of the DESHIMA instrument, developed to enable high-sensitivity measurements of astronomical sources. The primary objective of DESHIMA 2.0 is to study high-redshift galaxies by detecting faint emission lines, such as the ionized carbon ([C II] 158 μm) line, which are redshifted into the submillimetre range due to the expansion of the universe [1][10]. To understand the performance of DESHIMA 2.0, it is important to first examine the workings of the spectrometer system itself, as well as the components that make up the DESHIMA system.

2.1.1. Instrument Design and Components

The DESHIMA 2.0 instrument is deployed on the ASTE (Atacama Submillimetre Telescope Experiment) 10-meter telescope. ASTE is a submillimetre observatory located in the high-altitude desert of northern Chile, an optimal site for reducing atmospheric interference. DESHIMA 2.0 is equipped with a two-beam setup, which allows for rapid switching between the sky (the atmosphere) and an astronomical source. The reasons for implementing this two-beam setup are explained in more detail in Section 2.3.

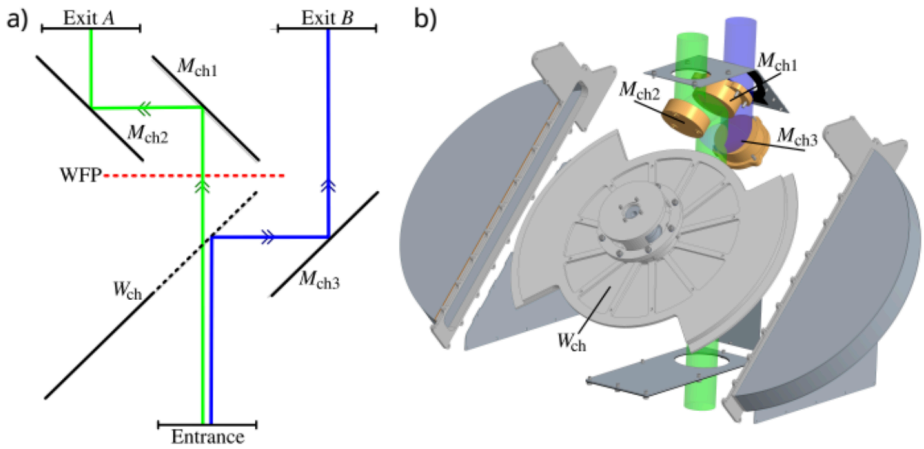

Figure 2.1: (a) Schematic that shows the chopper wheel is able to switch between beam a and beam b. (b) Side view of the chopper. Please note that the green and blue tubes are not an accurate representation of the beam; they are used only for demonstration purposes. Figure from Moerman et al., in prep.

Figure 2.1 illustrates how a chopper wheel switches between beam a and beam b, enabling observations of two different positions in the sky. The primary objective of this switching is to filter out noise caused by atmospheric fluctuations and instrumental drifts. By rapidly alternating between these positions at a rate of 10 Hz, the chopper effectively reduces the impact of these noise sources on the observations. This method also minimizes dead time during observations, as it eliminates the need to physically move the telescope between the two positions, making it more efficient compared to nodding the telescope alone.

An important consideration when using the chopper wheel is that, as it rotates to switch between beam a and beam b, there are moments when the wheel partially intercepts the beam. During these moments, part of the signal may be diffracted, spilling over to the warm interior of the chopper or to the ground. This diffraction can result in significant spikes in the received signal, which must be removed through postprocessing the measured data (a process known as ”despiking”). This issue, along with its mitigation strategies, is discussed in Section 2.3.

Additionally, a tilt in the chopper wheel can introduce further challenges. In earlier analyses, an offset in T_b (brightness temperature) has been observed in beam b between subsequent positions. This offset may result from a small tilt in the chopper blade's normal relative to its axis of rotation, causing the blade to precess as it spins [18].

If there is tilt in the chopper blade, one half will experience a positive tilt while the other half experiences a negative tilt. This can lead to variations in spillover, either inside the sky chopper or towards the ground. Consequently, one beam may interact more with warmer regions—such as the sky chopper interior or the ground—than the other, resulting in noticeable brightness temperature offsets [18]. Even minor spillover differences can significantly affect the signal due to the power contribution from these warmer regions. When filtering out atmospheric noise, it is therefore crucial to account for these spillover-induced effects to properly address any systematic issues during postprocessing.

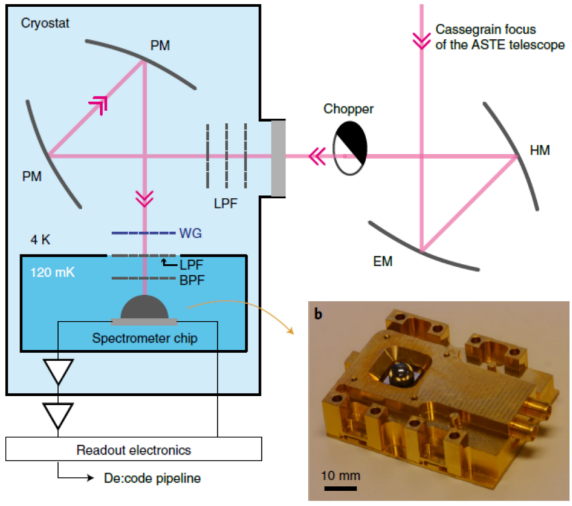

Figure 2.2: DESHIMA 2.0 in the ASTE telescope cabin (a) The sub-mm signal from the ASTE telescope is guided to the ISS chip through a series of mirrors, filters, and a polarizer, with MKID responses read out at 160 Hz (b) The ISS (Integrated Submillimetre-Spectrum) chip [10]

Figure 2.2 shows the cryostat used in the ASTE telescope. Light enters the system through the chopper and is guided along the optical path that focuses the incoming radiation onto the antenna. To achieve the required sensitivity, the DESHIMA 2.0 instrument is housed within a cryostat that cools the detectors to 120 mK. This cryogenic environment significantly reduces thermal noise, enabling the superconducting detectors to operate near the photon-noise limit. Such a setup is crucial for achieving the high sensitivity needed to detect faint astronomical signals [10].

2.1.2. Microwave Kinetic Inductance Detectors (MKIDs)

The core of the DESHIMA 2.0 instrument is its spectrometer chip, which among other components consists of many microwave kinetic inductance detectors (MKIDs). These detectors are integrated with a filter bank that covers the entire 200–400 GHz frequency range. Simply said, they function by detecting shifts in resonance frequency caused by the absorption of incoming photons. When a photon is absorbed, it alters the kinetic inductance of the superconducting material, leading to a measurable shift in the resonance frequency of the detector. Deeper understanding of the superconducting properties of the chip is beyond the scope of this report and won't be discussed further.

Figure 2.3 shows DESHIMA 2.0's chip which features 347 spectral channels, each tuned to a specific frequency band, allowing for the capture of a wide-band spectrum in a single observation. The filter bank spans a frequency range of 200–400 GHz, with each filter designed to pass specific frequencies [1]. However, it is important to note that the filters are designed to pass signal at their fundamental resonance frequency, but they will also pass signal at their higher-order harmonic resonance frequencies. For example, a filter set for 200 GHz can detect frequencies at 400 GHz and other higher-order multiples. This characteristic must be considered during data analysis, as lower-frequency filters may inadvertently capture signals from higher frequencies, which could affect the interpretation of the data.

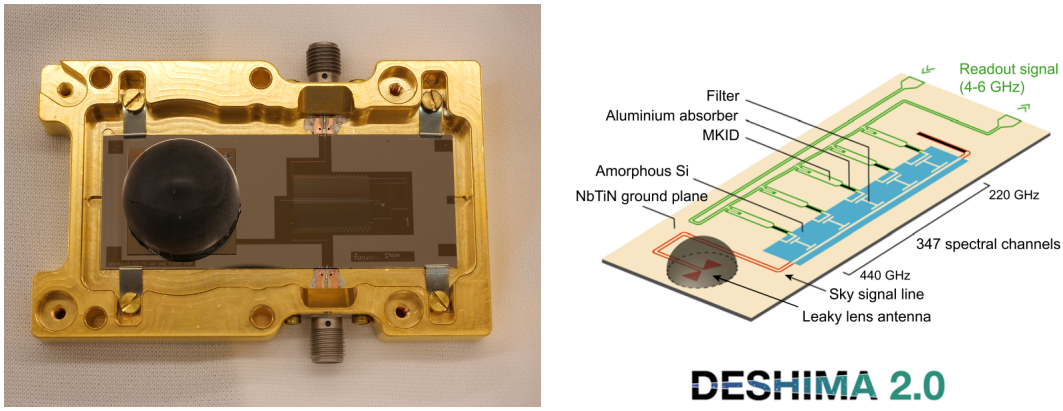

Figure 2.3: Chip of DESHIMA 2.0, on the left a picture and on the right a schematic showing the filter bank with 347 channels [1].

This design enables simultaneous observation across a broad frequency range, facilitating the detection of multiple emission lines. Furthermore, it allows for the detection of emission lines from distant galaxies with unknown redshifts, providing valuable insights into the galaxies' redshift values in a single observation [1].

2.2. Noise Sources and Characteristics

For ground-based observations like those conducted with the ASTE telescope, the signal we receive consists of both the spectrum from the astronomical source and contributions from other sources. One major contribution is the average power received from the Earth's atmosphere, which can be more than 10,000 times brighter than the astronomical signal. The challenge arises because atmospheric power fluctuates over time, introducing noise into the signal. This variability makes it more difficult to filter out the atmospheric contribution, as it is continuously changing.

In this report, we will discuss two types of noise that affect the analysis of observations: photon noise and atmospheric noise caused by the time-varying component of the atmosphere. Understanding these noise sources, particularly how to filter out atmospheric noise, is essential for improving the clarity of the astronomical signal.

2.2.1. Atmospheric Noise

Submillimetre galaxies (SMGs) are typically faint in optical wavelengths but emit bright thermal radiation in the far infrared, making this range the most effective for detecting and studying them. However, the Earth's atmosphere poses challenges for such observations: its strong infrared absorption reduces the signal reaching the telescope, while its emission contributes to noise in the measurements. Together, these atmospheric effects significantly impact the signal-to-noise ratio (SNR), with absorption decreasing the signal (S) and emission increasing the noise (N).

The transmission of infrared radiation through Earth's atmosphere varies with atmospheric composition, particularly with water vapour levels, which fluctuate both spatially and temporally [22]. These fluctuations impact observations in the sub-mm and THz ranges, such as the 200–400 GHz range targeted by the DESHIMA 2.0 spectrometer. The atmosphere's transmission and absorption rates are non-linear across these frequencies, complicating the task of filtering out atmospheric noise. Water vapour, in particular, absorbs sub-mm radiation, creating absorption bands that can severely hinder detection of faint extragalactic sources. Therefore, observatories are often located in high-altitude regions like the Atacama Desert to minimize water vapor content; the ASTE site, situated 4,860 meters above sea level, frequently experiences precipitable water vapour (PWV)[1] levels below 1 mm, providing a more favourable observational environment.

Temporal and spatial variations in the atmosphere significantly complicate astronomical observations in the sub-mm spectrum. Temporal variations, such as changes in water vapour and temperature over time, affect both the transparency of the atmosphere (how much light can pass through) and the intensity of its own emission, with the latter being a major contributor to noise. These variations are inherently linked to spatial differences, as dynamic processes like wind move water vapour and other atmospheric properties across the sky. For instance, wind can cause rapid, uneven changes along the line of sight, making it difficult to predict and correct for atmospheric effects. These fluctuations introduce noise and reduce the reliability of measurements, complicating efforts to isolate the faint signals from distant galaxies [12].

To address this noise, a technique known as "sky chopping" can be used. By rapidly switching the telescope's beam between the target source and a nearby blank region of the sky, we can measure the difference in signals to reduce the atmospheric contribution. A more detailed explanation of how this is done in the ASTE telescope will be discussed in section 2.3.

2.2.2. Photon-noise

In addition to atmospheric noise, photon noise is another important factor to consider. Photon noise arises from the random, statistical nature of photon arrivals at the detector. In submillimetre (sub-mm) astronomy, photon noise is a major source of signal fluctuation, as photons arrive discretely over time. The rate of photon arrival is inherently random, meaning that the time intervals between detections vary, leading to signal fluctuations [9] [23]. This randomness follows Poisson statistics, where the number of photons detected in a given time period follows a Poisson distribution. Poisson noise is dominant when the signal is weak. However, as the signal gets stronger, another phenomenon, known as photon bunching, begins to play a role. Photon bunching occurs when photons tend to arrive in groups rather than independently. As the signal increases, photon bunching becomes more noticeable, contributing additional noise to the total signal.

The total NEP can be expressed by the following equation [4][9]:

$$NEP_{ph} = \sqrt{2P(hf + \frac{P}{\Delta\nu}) + \frac{4\Delta_{Al}P}{\eta_{pb}}} \tag{2.1}$$

In this equation, NEP is the Noise Equivalent Power, P is the power of the signal, h is Planck's constant, $\Delta\nu$ is the bandwidth, and f is the frequency. The first term under the square root represents Poisson noise, while the second term corresponds to photon bunching. This equation illustrates how the noise

[1] Note that PWV represents the total amount of water vapour in the atmosphere above a given location, expressed as the height of the water column that would result if all the vapour were precipitated as rain [20].

scales with power: as the signal power increases, photon bunching becomes more significant, whereas at lower powers, Poisson noise dominates.

The final term in the equation accounts for recombination noise, which is an intrinsic property of any quantum detector. Recombination noise is related to the process by which broken Cooper pairs in the detector recombine, contributing to fluctuations in the detected signal. In the equation, Δ_{Al} represents the superconducting gap energy of aluminium, and η_{pb} is the pair-breaking efficiency. While the exact mechanism of recombination noise is not central to this discussion, its inclusion in the total NEP reflects its role as a part of the overall photon noise (together, with the Poisson noise and photon bunching).

When a signal is said to be ”photon-noise limited,” photon noise becomes the dominant source of noise, surpassing other types of noise, such as thermal or electronic noise from the detector, or atmospheric noise. This condition is ideal for high-sensitivity measurements, as it indicates that the received signal is only limited by the statistical nature of light itself, rather than additional noise from the instrument or the environment. In photon-noise-limited conditions, improving the detector will not enhance sensitivity, as the signal's noise floor is already set by the fundamental statistics of photon arrival.

2.2.3. Integration Time and Noise Reduction

It can be very useful to examine how our signal (and its noise) behaves as we increase the integration time. This can help us understand how noise behaves as we average the signal over longer periods. If the noise is random and evenly distributed around a mean value, averaging will reduce its variability [11]. This reduction follows a proportionality where the standard deviation, σ, scales inversely with the square root of the integration time [19][13]:

$$\sigma \propto t^{-0.5} \tag{2.2}$$

Averaging over longer periods reduces the variability of random fluctuations, which improves the signal-to-noise ratio. As a result, as the integration time increases, the uncertainty in the measurement decreases, allowing weaker signals to become detectable. It enables the observation of faint cosmic sources by extending integration times to accumulate a sufficient signal compared to the noise level.

However, real-world measurements may include noise patterns that do not diminish as expected with averaging, leading to deviations from this ideal behavior. By studying the standard deviation of the noise at different integration intervals, we can identify when these deviations occur and evaluate the limits of our measurement system. This insight is crucial for determining the optimal integration time to observe weak signals without being misled by persistent noise components.

2.3. Techniques for Noise Mitigation

Chopping, also known as beam-switching, is an essential technique for ground-based observations, used to minimise noise in the signal and approach the photon-noise limit. This method helps to eliminate the atmospheric contribution to the signal and correct for systematic errors.

The process involves observing two separate points in the sky: the ON position (where the astronomical source is located) and the OFF position (where no source is present) [24]. The angle between these points is known as the beam separation. This separation must be large enough to ensure no overlap between the two points in the far-field (where the source should be isolated in one position) but also close enough in the near-field so that the atmosphere remains nearly identical between the two positions. The maximum beam size at the lowest frequency is about 30 arcseconds [16], and the separation between the two positions is set to 233.6 arcseconds (see Figure 2.4). This distance is at least seven times the beam size, ensuring that there is no overlap between the two beam positions in the sky.

This technique can help reduce atmospheric noise. As shown in Figure 2.4a, with proper beam separation in the far-field, the beam passes through almost the same cylinder of atmosphere, meaning the atmospheric conditions are spatially similar. Figure 2.4b further demonstrates that, temporally, atmospheric fluctuations are minimal in the near-field. By subtracting the signal in the OFF position from the

ON position, the atmospheric signal is effectively filtered out, leaving only the signal from the distant galaxy.

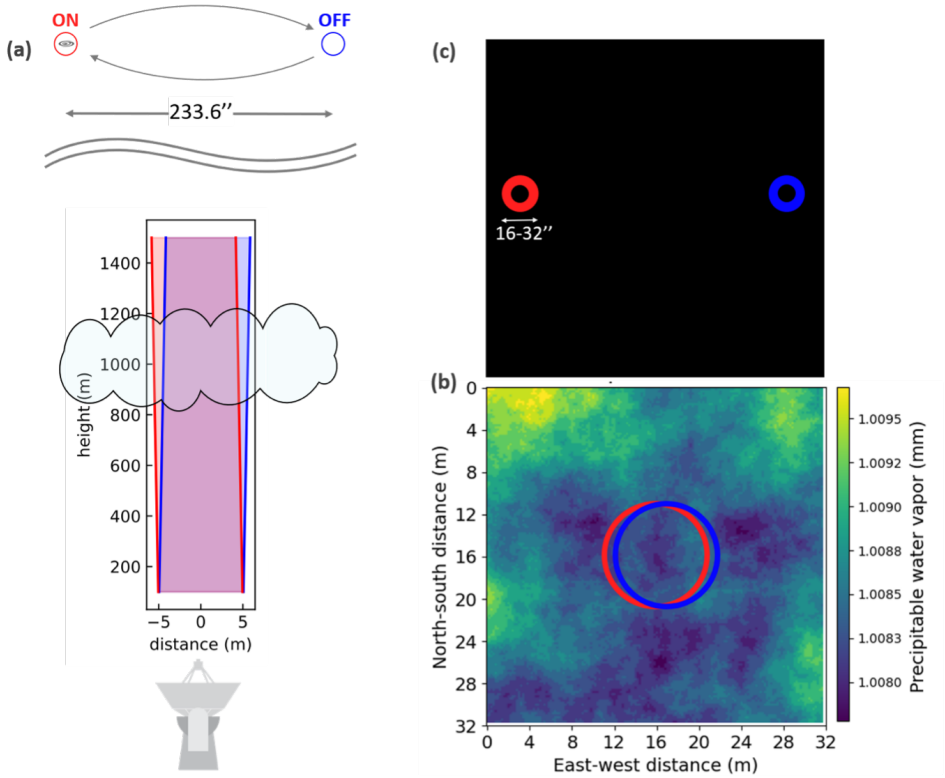

Figure 2.4: Schematic diagram illustrating the ON and OFF positions during chopping. (a) shows how, in the near field, the beam passes through almost the same volume of atmosphere, while in the far field, it observes two distinct positions in the sky. (b) shows the separation in the near field, demonstrating how the two beams pass through approximately the same atmospheric conditions. (c) shows the separation in the far field, further illustrating how the two beams correspond to clearly different positions on the sky[12].

2.3.1. ABBA Chopping: Principles and Implementation

To effectively filter out atmospheric noise from a signal, we use a technique called ABBA chopping. As discussed in Section 2.1, the telescope is equipped with a rotating mirror, which allows for continuous switching between two beams, a and b. This switching enables us to subtract the signal in the OFF position (in beam b) from the signal in the ON position (in beam a), thereby isolating the astronomical source. ABBA chopping improves this process by adding a more sophisticated approach.

In ABBA chopping, instead of keeping the source fixed in beam a while leaving beam b empty, the telescope is moved every minute to alternate the position of the source between the two beams. In Figure 2.5, we define ”Nod A” as the position where the source is located in beam a and ”Nod B” as the position where the source is located in beam b. Throughout the observation, the telescope continuously alternates between Nod A and Nod B, with each nod occurring every minute. Given that the mirror rotates at 10 Hz (actually rotates at 5Hz, but due to the shape of the chopper wheel, allowing two beam a and two beam b positions per rotation, the a/b oscillates at 10Hz, see Figure 2.1 in section 2.1), this results in 600 chops per Nod.

The advantage of ABBA chopping lies in how we process the data to remove atmospheric noise (and systematic noise). Instead of simply subtracting all the off-source values from the on-source values, as we did earlier, the nodding allows us to alternate the subtraction: first subtracting the signal in beam b from the signal in beam a (a-b), and then reversing the process by subtracting the signal in beam a from the signal in beam b (b-a). This alternating process helps to more effectively cancel out atmospheric fluctuations and improves the quality of the signal. The following plots will further illustrate how this works.

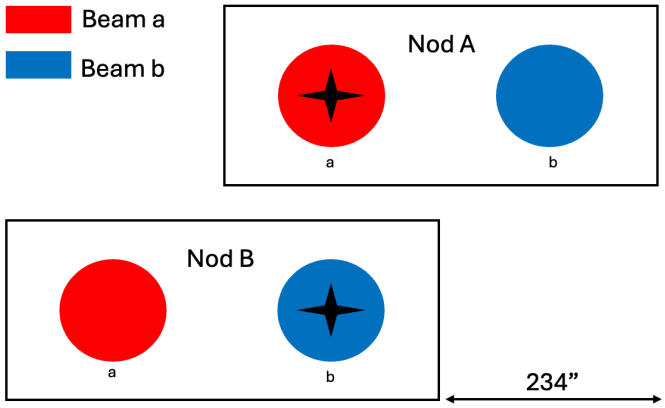

Figure 2.5: Schematic diagram to show the positions of beam a and beam b in Nod A and Nod B

The ABBA chopping pattern (a-b, b-a, b-a, a-b) is preferred over patterns like ABAB because it alternates the observation sequence, helping to cancel out systematic changes in atmospheric or instrumental conditions over time. By reversing the AB order to BA (instead of repeating AB AB), ABBA more effectively reduces steady or gradual changes in the atmosphere and instrumentation. In comparison, ABAB repeats the same sequence, increasing its vulnerability to residual noise from changing conditions. This makes ABBA a more reliable choice for minimising noise in dynamic environments [24].

There are different methods for applying ABBA chopping, with key differences depending on whether you first perform the a-b (and b-a) subtractions or first calculate the mean value of a certain number of chops. In this report, we first perform the subtractions between individual chops before calculating the average of a segment or cycle.

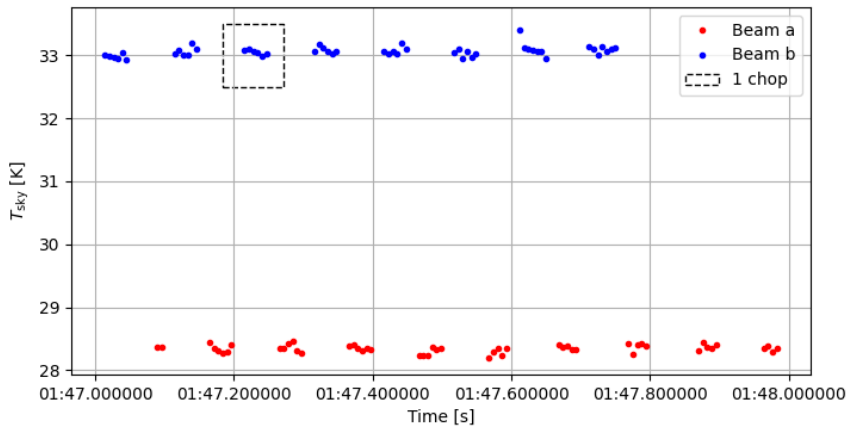

Figure 2.6: Tsky versus time for a very short time range of 1 second to illustrate how one chop is defined. Note that at this time during the observation the source is in beam b. Also note that the data has already been despiked.

The first step is to split the data into a and b chops. Figure 2.6 shows an example where beam b (blue points) is on source and beam a (red points) is off source. A chop is defined as the group of points within the black box shown in the figure. On average, there are 8 data points per chop. After splitting the data into chops, it is ”despiked” by removing the first and last points of each chop, which accounts for the mirror still being partially in the beam, as discussed in Section 2. Once the despiking is complete, the mean value of each individual chop is calculated. For an atmospheric observation lasting 3000

seconds, we are left with 31,362 chops for beam a and 31,362 chops for beam b [2].

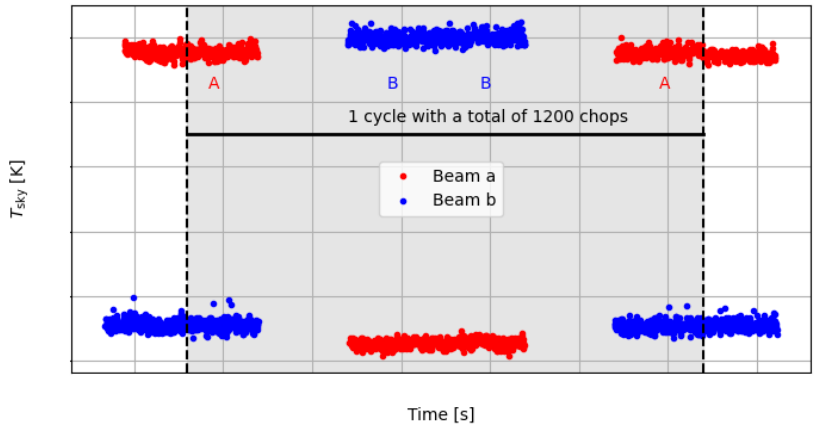

Figure 2.7: Tsky versus time. The shaded area is 1 complete ABBA cycle. Note that this data has already been despiked.

The next step is to calculate the number of ABBA cycles. As shown in Figure 2.7, one ABBA cycle consists of half of Nod A, Nod B, and then half of Nod A again. Each half of a Nod is referred to as a "segment," so Nod A consists of two A segments. Since each Nod contains 600 chops, one ABBA cycle contains 1200 chops. This is illustrated in Figure 2.7 as the area shaded in grey. To determine the number of ABBA cycles, we divide the total number of chops by 1200. For the atmospheric observation, this means 31,362 chops divided by 1200 = 26.135 cycles. To ensure we work with a whole number of cycles, we consider only the first 26 cycles, ignoring the remaining 0.135 cycle.

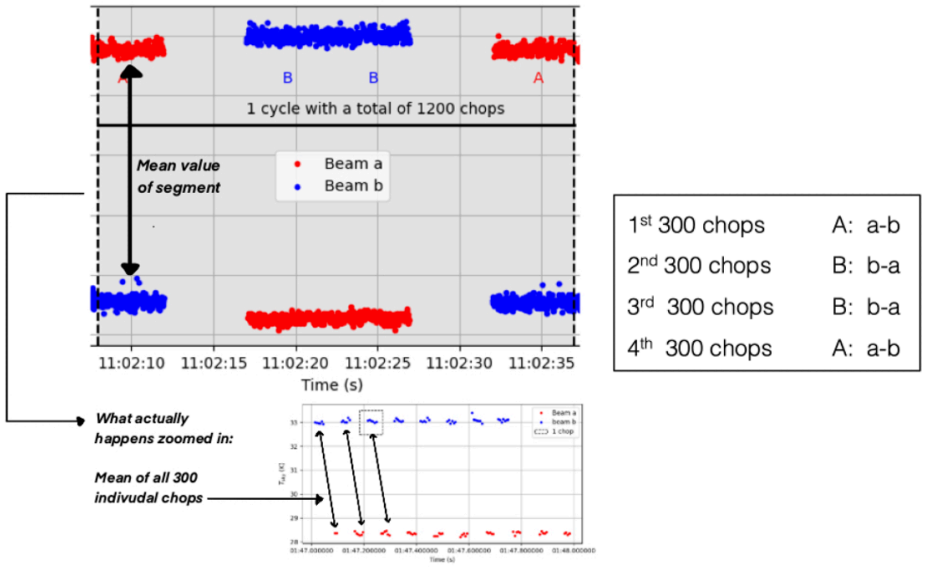

Figure 2.8: Diagram to illustrate how the chopping is performed. First the individual subtractions are done for each chop, and then the mean value is taken.

Now that we know how many ABBA cycles there are in our observation, we can start doing the subtracting according to the appropriate "pattern". As mentioned earlier a segment is known as half a Nod,

[2]Note that with 31,362 chops the observation is actually a bit longer than 3000s. You would expect 30,000 chops for a 3000s observation. This is because extra data was recorded before and after the 3000s observation (labeled as "SCAN" in the measurement file).

which means there are 300 chops per segment. For each 300-chop segment, we perform the subtraction between beam a and beam b (or vice versa). After performing the subtraction for each individual chop, we calculate the mean value of the 300 subtractions, as shown in Figure 2.8. This results in a mean value for each segment. To find the final mean value for the ABBA cycle, we take the mean of the four segments.

By repeating this ”pattern” for all 26 ABBA cycles, we try to obtain the spectrum of our signal with the atmospheric noise filtered out. Since we alternate between a-b and b-a subtractions, we aim to effectively filter out any systematic errors.

2.4. deshima-sensitivity

To develop an analytical model for sensitivity based on laboratory measurements, the Python package deshima-sensitivity is used [8]. This tool calculates the spectrometer’s sensitivity by incorporating a wide range of input parameters.

The main function of deshima-sensitivity is to model the spectrometer’s sensitivity by calculating the Noise Equivalent Temperature (NET), useful for evaluating detection limits (discussed further in Section 3.4). The package takes inputs such as spectrometer characteristics (e.g., filter center frequency and spectral resolution), efficiency factors (e.g., circuit efficiency), and atmospheric conditions (e.g., telescope elevation angle and precipitable water vapor). Based on these inputs, it generates a sensitivity model for DESHIMA-type spectrometers, referred to as the photon-noise model. To calculate photon noise, the package uses Equation 2.1. Atmospheric effects are accounted for using an ATM model[3].

For this report, NET serves as the most relevant sensitivity measure and will be used extensively in subsequent analyses. Furthermore, deshima-sensitivity also calculates atmospheric transmission, using parameters such as frequency, precipitable water vapour (PWV) [21], elevation angle, and spectral resolution (R) (also based on the ATM model). This function is essential and will be applied further in Chapter 3.3.

3

Instrument Characterisation and Theoretical Modelling

3.1. Laboratory Measurements

Before DESHIMA 2.0 was installed on the ASTE telescope, laboratory measurements were conducted to ensure that everything was functioning as expected. Key properties of each frequency channel of the DESHIMA 2.0 chip, such as the filter center frequency (F), spectral resolution (Q), and optical efficiency (η), were measured in the lab.

From the lab measurements, two sets of efficiencies were recorded: one derived from hot and cold measurements and another from observations of a coherent source. Both are shown in Figure 3.1. For constructing the model, the efficiency derived from the coherent source is used, as it most closely reflects the conditions during telescope observations.

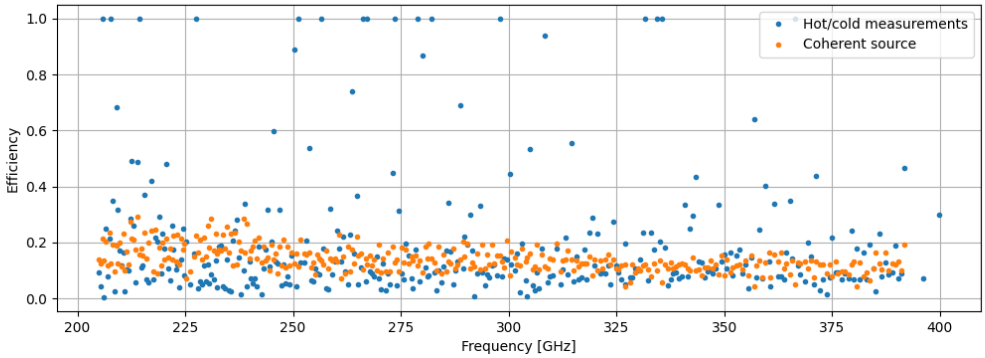

Figure 3.1: Measured efficiencies for all frequency channels.

To ensure accuracy in the analysis, it is essential to label all detector-specific parameters (F, Q, η) with the ”master ID” of their respective frequency channels. This is important because it enables a channel-to-channel comparison between the model and actual observations. During the comparison, parameters with the same master ID can be directly matched to evaluate the extent to which they agree or differ.

Using the deshima-sensitivity package (discussed in Section 2.4), we can construct a model that assumes photon-noise-limited sensitivity. While the detector-specific parameters (F, Q, η) are central to this model, it also requires observation-specific input parameters to simulate actual telescope conditions. These include the precipitable water vapour (PWV) and the telescope’s elevation angle (El),

which must match the conditions of the observations being analysed. For comparisons with observations conducted without chopping, this condition must also be reflected in the input parameters. For instance, to model an atmospheric observation where the telescope remains stationary with the chopper off, at an elevation of 60º and PWV of 1.0 mm, we use the input parameters listed in Table 3.1. This allows the creation of a model that accurately reflects photon-noise-limited sensitivity under these specific observational conditions.

Input parameters	
F	Filter center frequency
pwv	1.0
El	60.0
R	Spectral resolution
eta_circuit	Efficiency
on_off	False

Table 3.1: Input parameters for deshima-sensitivity to create photon-noise model, this one specifically to model an atmosphere observation with the chopper wheel off.

3.2. Beam Measurements

Beam measurements conducted by Arend Moerman are a critical component of the analytical model, especially when examining an astronomical source. He used Mars observations from July 13-18, 2024, to calculate the solid angle, main beam efficiency, and aperture efficiency [16].

The beam measurements on the ASTE telescope are made by observing Mars and applying a series of models and corrections. A disk-convolved Gaussian function is first fitted to the beam profile, which allows for the calculation of the Full Width at Half Maximum (FWHM) in both the x and y directions, providing the resolution of the beam (Figure 3.2).

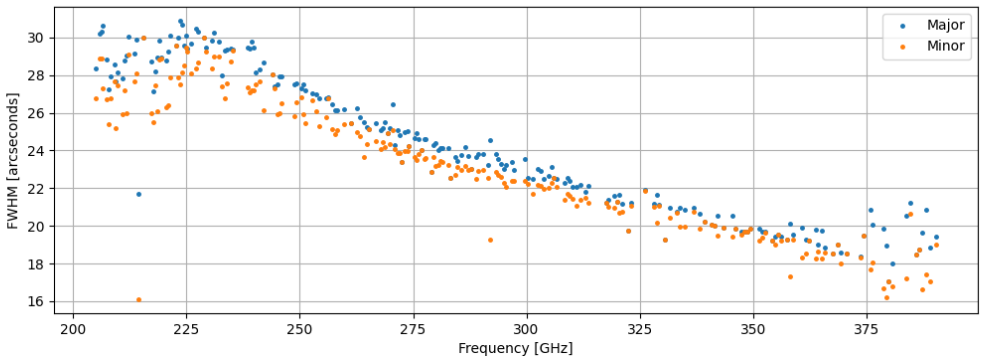

Figure 3.2: Full Width at Half Maximum (FWHM) in both x and y direction for each individual channel.

A model of Mars' brightness temperature is used to compute the antenna temperature, and the solid angle subtended by Mars is incorporated into the calculations. This solid angle is important for converting the observed signal into a brightness temperature.

Atmospheric conditions, including the precipitable water vapour (PWV) data during the scan, are taken into account to adjust for atmospheric effects. The main beam efficiency is then determined, with elevation corrections factored in. This efficiency is calculated using the model of Mars's brightness temperature and the antenna temperature, adjusted for the telescope's elevation during the scan.

Next, the aperture efficiency is calculated using the main beam efficiency and the physical aperture area of the telescope, as well as the observation wavelength. The aperture efficiency reflects how well the telescope collects and focuses incoming waves, based on the physical area of the ASTE telescope's aperture. This is summarised in the equation below [16]:

$$\eta_{ap} = \frac{\lambda^2 \eta_{mb}}{A_p \Omega_{mb}} \tag{3.1}$$

This process ensures accurate measurement of the telescope's performance by considering both instrumental and atmospheric factors, with Mars serving as the calibration source. The aperture efficiency obtained is particularly relevant when comparing the spectrum of an astronomical source observation to a known model of the spectrum.

3.3. Modelling Atmospheric Sky Temperature

Sky temperature is the apparent temperature of the sky as observed from a telescope on the ground. It refers to the thermal radiation emitted by the atmosphere and various components of the sky, including water vapour and the cosmic microwave background (CMB). Sky temperature is an important parameter in astronomy because it contributes to the "noise" in the observed signal, as discussed in Section 2.2.1.

Sky temperature can vary based on atmospheric conditions such as precipitable water vapour (PWV), wind, and the elevation of the observation site. It is commonly expressed in brightness temperature, which represents the equivalent temperature of a perfect blackbody that emits the same amount of radiation at a particular frequency [7]. The sky temperature is defined as [10]:

$$T_{\text{sky}} = T_{\text{ground}} \left(1 - \eta_{\text{atm}}\right) \tag{3.2}$$

In this equation, T_{ground} is typically approximated as 270 K, and η_{atm} is the atmospheric transmission factor. η_{atm} can be determined using a function in the 'deshima-sensitivity' packaged. The "eta_atm_func" function calculates the atmospheric transmission (η_{atm}) as a function of frequency (F), precipitable water vapour (pwv), and telescope elevation (EL). It uses an interpolation method based on atmospheric transmission data from an ATM Model [3] and can smooth the transmission according to the spectral resolution (R).

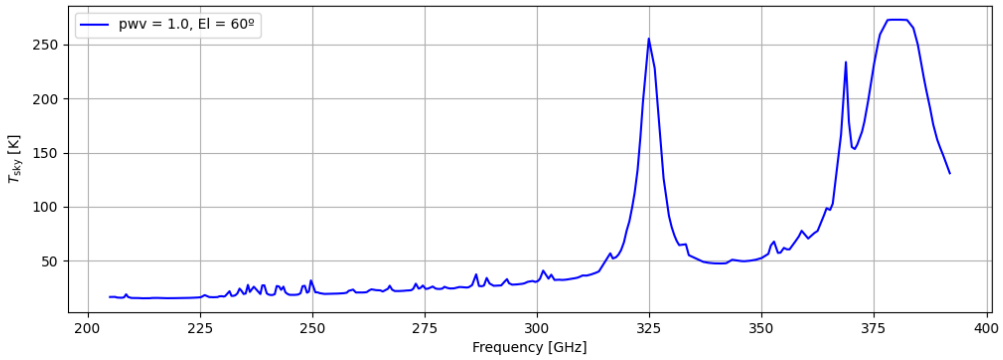

Figure 3.3: T_{sky} against frequency for each individual channel calculated using equation 3.2, where (η_{atm}) is found using "eta_atm_func" from the deshima-sensitivty package based on the parameters from Table 3.1 in section 3.1

The parameters described in Section 3.1 are used to calculate the sky temperature and are shown in Figure 3.3. Notably, for frequencies of 325 GHz and 380 GHz, we observe peaks in the plot, indicating very low atmospheric transmission ($\eta_{\text{atm}} \approx 0$), meaning $T_{\text{sky}} \approx T_{\text{ground}}$. This is an important consideration, as we expect similar behavior to be reflected in the observations presented in Section 4.

3.4. Noise Equivalent Temperature

Throughout this report, we will compare the Noise Equivalent Temperature (NET) of different atmospheric observations to the model created in Section 3.1. The Noise Equivalent Temperature (NET) is a measure of the telescope's sensitivity in detecting weak signals. It represents the minimum temperature change in the sky that can be detected with a signal-to-noise ratio (SNR) of 1, after an integration time of 1 second. An SNR of 1 means that the signal and noise have the same magnitude, indicating the threshold at which the signal can be distinguished from the noise. To create the photon-noise model, the NET will be found using the deshima-sensitivity package discussed in section 2.4. This is done using the following equation:

$$NET_{sky} = \frac{NEP_{kid}}{\sqrt{2}_{Hz\leftrightarrow s}} \frac{\eta_{IBF}}{\eta_{ins}\eta_{for}} \frac{R}{F} \tag{3.3}$$

The η's represent different efficiencies that are calculated in the dehsima-sensitivity package based on the parameters defined in Appendix B and the factor $\sqrt{2}$ accounts for a unit conversion between Hz and s.

3.4.1. Power Spectrum Density

The second method for calculating the NET involves examining the Power Spectral Density (PSD) of a signal. This approach is particularly relevant when determining the NET for a signal obtained from actual observations. To calculate the PSD, we use the '$signal.welch$' function from Python's '$scipy.signal$' module. This function estimates the PSD of a signal, quantifying how its power is distributed across different frequencies. In simple terms, it is based on the Welch method [26], which divides the signal into overlapping segments, applies a window function to reduce distortions, computes the power spectrum for each segment, and averages the results to produce a smoother, more accurate PSD estimate. The function returns the frequency values and the corresponding PSD estimates.

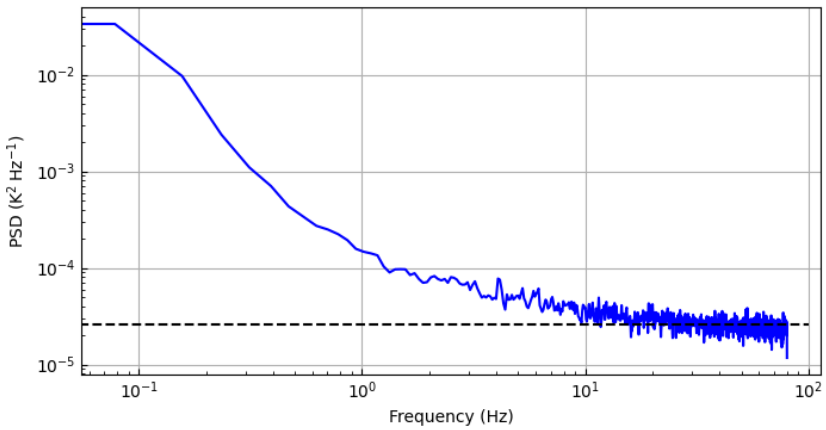

Figure 3.4: The power spectral density (PSD) is plotted against the frequency in Hz. The blue curve represents the PSD for a single channel (channel 200) from an atmospheric observation, while the dashed black line indicates where the curve flattens as photon noise begins to dominate over atmospheric noise.

In this analysis, signal.welch is used to calculate the PSD for all of DESHIMA's channels, sampled at 160 Hz. Parameters such as the segment size (nperseg) determine the resolution of the estimate, and overlapping segments improve accuracy. When examining the PSD of a single channel, two distinct regions can be identified. The first region, dominated by atmospheric noise, is characterized by 1/f noise [6], caused by the dynamic nature of the atmosphere. Beyond approximately 1 Hz, photon noise begins to dominate. This appears as a flat section in the high-frequency part of the PSD as illustrated in Figure 3.4.

To determine the NET, we calculate the variance of the PSD above 10 Hz, ensuring we are in the photon-noise-dominated range. The NET value is then the square root of this variance. Throughout this report, NET values are expressed in units of [mKs$^{0.5}$], and the result is divided by a factor of $\sqrt{2}$ to account for the unit conversion between Hz and seconds. This process is performed for each individual channel to compute the NET for all channels.

3.5. Photon-noise model

Using the 'deshima-sensitivity' package, as discussed in Section 2.4, along with the appropriate parameters from the lab measurements (detailed in Section 3.1), we can calculate the NET (using Equation 3.3). This process is carried out as described in Section 3.4, with all input parameters listed in the appendix B. The result is the NET for the photon-noise model, shown in Figure 3.5.

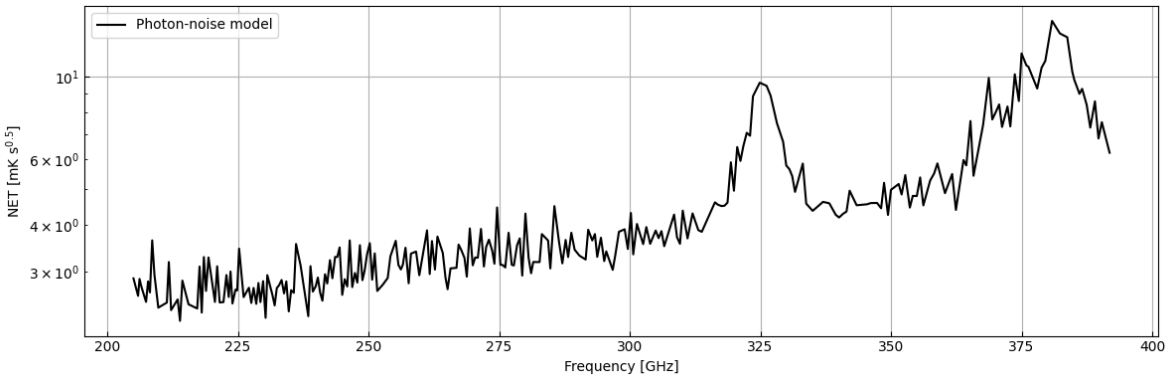

Figure 3.5: NET against frequency for the photon-noise model

This photon-noise model is referenced throughout this report to confirm photon-noise sensitivity during atmospheric observations. Two notable peaks appear at 325 GHz and 375 GHz, corresponding to regions of very low atmospheric transmission. These features, previously identified in Section 3.3 when discussing sky temperature, are also evident in the photon-noise model.

3.6. Mars spectrum Model

In this report, an observation of Mars will be conducted to further validate the spectral sensitivity and calibration of DESHIMA 2.0. The observed spectrum of Mars will be compared to its known spectral characteristics. To perform this comparison, a Mars brightness model is required [14]. Using specific input parameters (detailed in Appendix C), the flux density in Jy is calculated for given frequencies. To align the brightness model with the frequencies of DESHIMA 2.0, interpolation is performed. This process is illustrated in Figure 3.6.

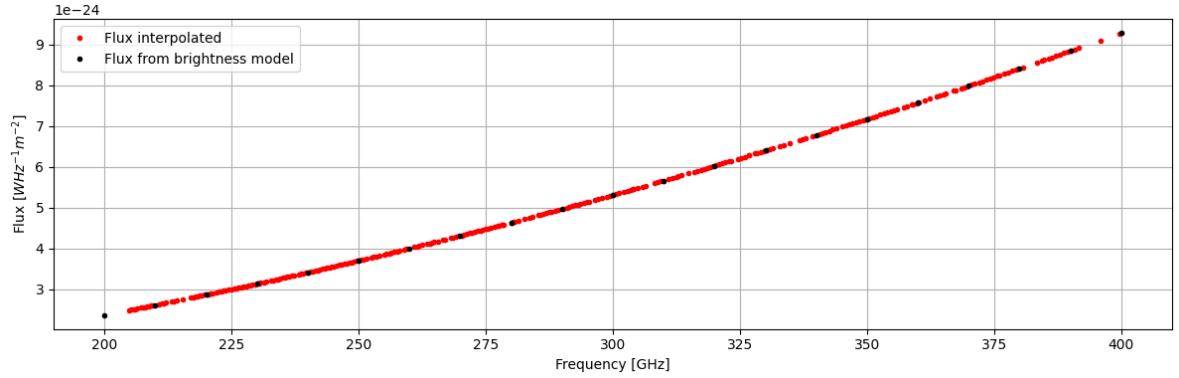

Figure 3.6: Plot showing the interpolation performed to make sure the frequencies of the mars brightness model align with those of DESHIMA 2.0

To compare the observed spectrum of Mars to the model, the flux density is converted into ΔT_{sky}. Here, ΔT_{sky} represents T_{sky} after performing the ABBA chopping analysis, where the signal is now isolated from the atmosphere. This flux density to ΔT_{sky} conversion is achieved using the following equations:

$$P = S_\nu A_e \Delta f \tag{3.4}$$

$$P = 2k_B T_A^* \Delta f \tag{3.5}$$

In these equations, P is the total power received by the telescope (in two polarizations), S_ν is the flux density of the source from the Mars model, and A_e is the effective aperture area, calculated as $A_e = \eta_A A_p$, where η_A is the aperture efficiency, and A_p, the physical aperture area of the telescope dish. In the second equation, Δf is the frequency bandwidth, k_B the Boltzmann constant, T_A^* the antenna temperature corrected for atmospheric attenuation and ΔT_{sky} the sky temperature after chopping, given by $\Delta T_{sky} = \eta_{atm} T_A^*$.

Figure 3.7 demonstrates this relationship between ΔT_{sky} and T_A^*.

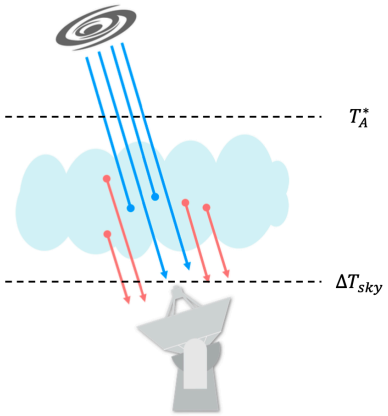

Figure 3.7: Diagram to show the difference between ΔT_{sky} and T_A^*. Diagram is from [12] however has been modified slightly.

When these are combined we get:

$$\Delta T_{sky} = \frac{S_\nu \eta_A A_p \eta_{atm}}{2k_B} \tag{3.6}$$

This equation allows the observed spectrum of Mars to be compared to its known spectrum. It is important to note that the factor of 2 arises because the flux density represents the two-polarization flux density of the source, as reported in the literature. Similarly, P represents the two-polarization power falling on the telescope dish. However, the DESHIMA chip is sensitive to only one polarization.

4

On Sky Observations

4.1. Observation Process and Data Collection

Observations for this project were carried out both remotely from TU Delft and on-site in San Pedro de Atacama (SPdA). Remote observations were done by logging into Amazon Workspace to access the ASTE control system, COSMOS3. This system allows users to control the telescope and run observing scripts, as shown in Figure 4.1. Each action, such as starting or stopping observations, was carefully logged to keep track of everything for later reference. After each observation, a quick-look analysis was done to create an initial image, which was also recorded in the observation log. Keeping detailed logs ensures that all data and any corrections are well-documented, making later analysis more reliable. Important factors during observations include monitoring weather conditions, like wind speeds, which must stay below 20 m/s, and making sure the telescope is not pointed within 25 degrees of the Sun to avoid damage and errors. On-site observations also required regular trips to the high site to transfer data using an SSD for further analysis. Collaboration between teams in Japan, Chile, and the Netherlands, makes it possible to observe continuously around the clock.

(a)

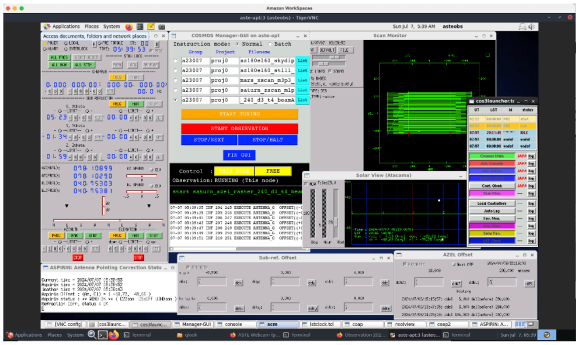

(b)

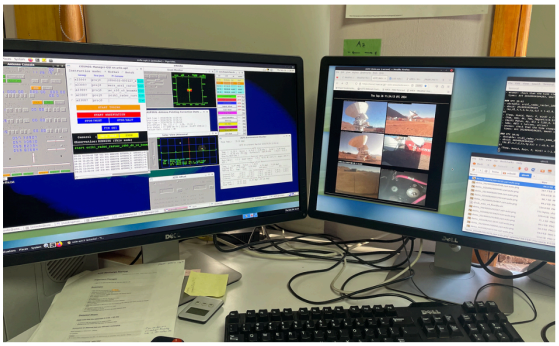

Figure 4.1: (a) COSMOS3 interface during a remote observation (b) Remote observation in progress: COSMOS3 control system (left) and live ASTE webcam feed (right).

I conducted observations both remotely at TU Delft and on-site in SPdA. For this report, the atmospheric data was collected directly through my own observations, while the Mars data came from observations made by colleagues. Atmosphere observations were conducted on October 1st, 2024. At 20:09 UTC, a still beam ab observation was performed, and at 21:10 UTC, a still beam a observation was conducted, each lasting 3000 seconds.

For the still observation, the term still refers to the telescope not moving. So for still beam a, the telescope observed the atmosphere at an elevation of 60º without any movement, using only beam a.

For the still beam ab observation, the telescope also remained stationary at the same elevation, but this time the chopper was activated, enabling observations with both beam a and beam b.

Additionally, two observations of Mars are analysed which were taken on September 21st, 2024, at 10:57 UTC and 11:04 UTC. Two observations are included in the analysis to verify consistency, as the results are expected to align. The observations used in this study are selected based on good KID correspondence (from the chip) and favorable weather conditions (PWV $\approx$ 1).

Figure 4.2 presents the time-domain data for the atmosphere observations. To compare these with the photon noise model, the raw data must first be processed, as described in Section 3.4.1. The processed results will be discussed below, starting with the still beam a observation in Section 4.2, followed by the still beam ab observation in Section 4.3.

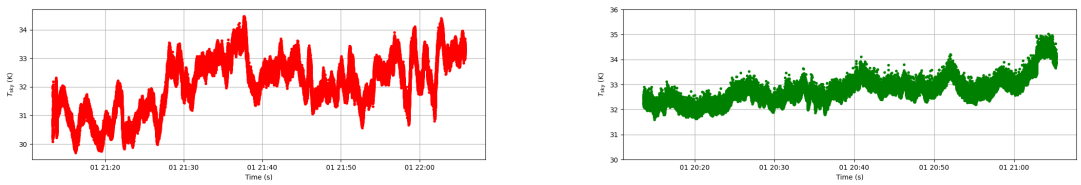

(a) (b)

Figure 4.2: Time-domain data from atmospheric observations. Note: The ”01” in the x-axis refers to the date (October 1st). (a) Time-domain data for a single channel from the still beam a observation. (b) Time-domain data for a single channel from the still beam ab observation.

4.2. Atmosphere: Still beam a

4.2.1. NET

We first analysed the still beam a observation of 3000 seconds. For each individual channel, the NET values were determined and compared to those predicted by the photon-noise model (described in Section 3.5). The NET was calculated by plotting the PSD for each channel and computing its variance beyond 10 Hz, as outlined in Section 3.4. This is shown in Figure 4.3.

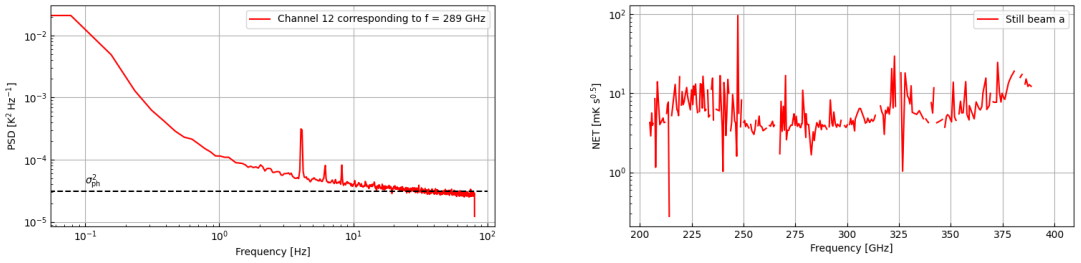

(a) (b)

Figure 4.3: (a) PSD for channel 12 for the still beam a observation, where the black line represents the variance after 10Hz. (b) NET for each individual channel of a still beam a observation.

The NET values found for beam a are compared to the NET from the photon-noise model as seen in Figure 4.4. Overall, the results agree well, but discrepancies are observed at lower frequencies, particularly below 250 GHz.

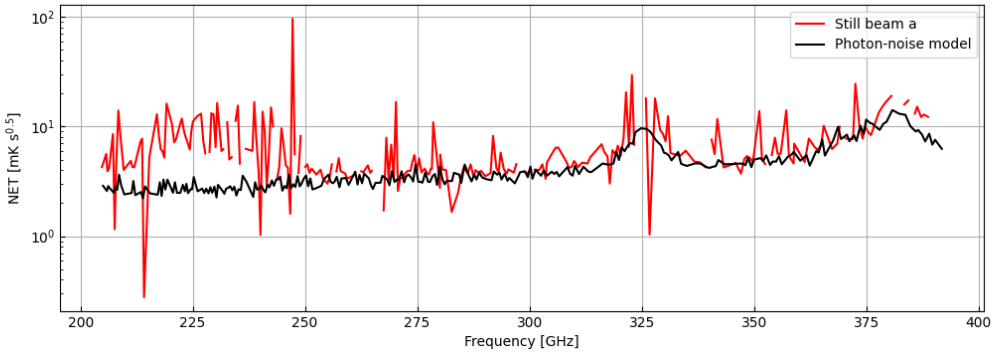

Figure 4.4: NET of a still beam a observation (red) compared to the NET of a photon-noise model (black).

At frequencies of 325 GHz and 375–390 GHz, we can see peaks in the NET that correspond to peaks observed in T_{sky}, (which also align with the photon-noise model). These peaks are associated with near-zero atmospheric transmission. For frequencies lower than 220GHz we know that the low frequency filters also pick up higher order frequencies which can explain these peaks at f<220GHz. However this doesn't explain the differences for the range between 220GHz and 250GHz . The individual PSD plots for each channel in that frequency range (shown in Appendix D) also do not show any unexpected or strange results. A possible explanation could be a calibration error at low frequencies which would occur in a vertical offset [2].

To better understand the correspondence, a channel-to-channel comparison was performed (Figure 4.5), revealing strong agreement between the still beam a observation and the model, particularly in the frequency range of 250–320 GHz.

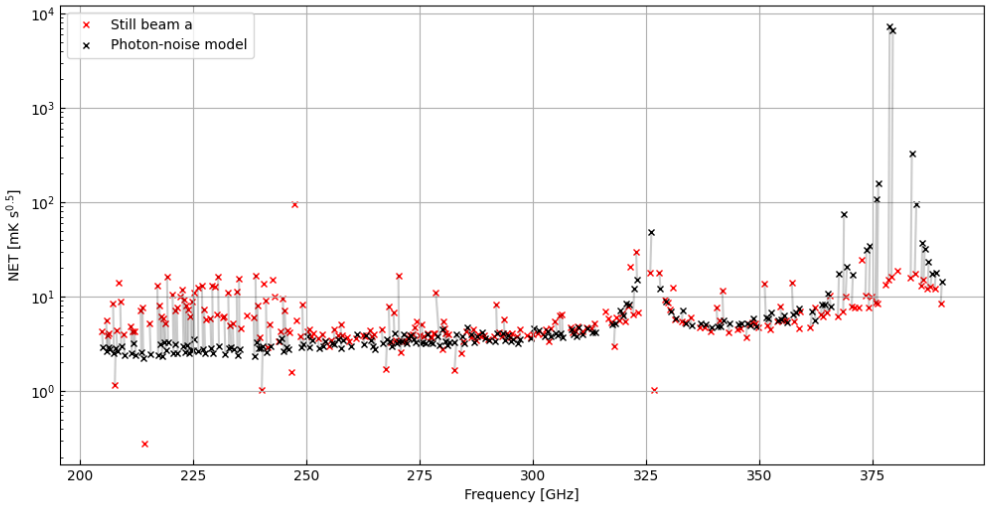

Figure 4.5: Channel to channel comparison for the NET of a still beam a observation (red) and the NET of a photon-noise model (black).

4.2.2. Noise in Spectrum

A second method for evaluating consistency with the photon-noise model involves analysing the spectrum and observing how the noise decreases with integration time. To do this, a simulated ON/OFF sequence was created by dividing the data into equal halves, assigning one half to "ON" and the other

to ”OFF,” followed by a simple ON-OFF subtraction. The remaining noise is the noise we expect due to photon noise.

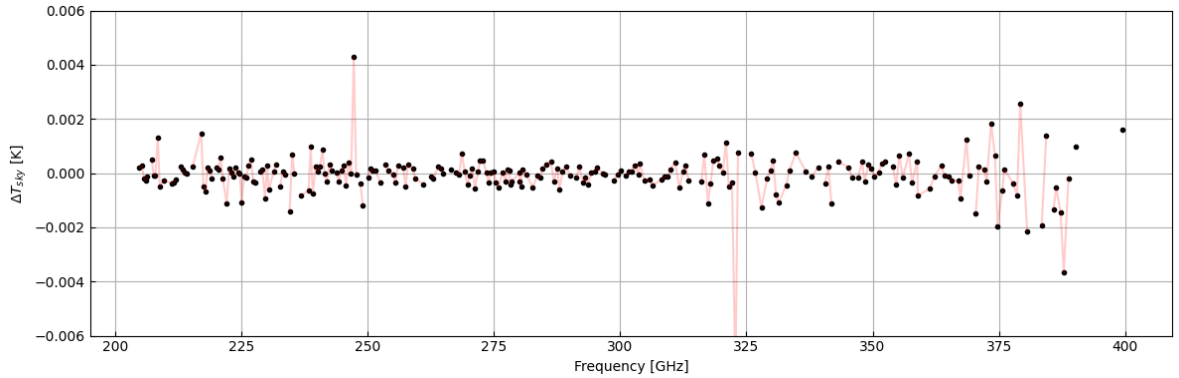

Figure 4.6: Noise in spectrum of a still beam a observation after simulating ON/OFF chopping.

Figure 4.6 shows the noise in the spectrum for the still beam a observation. Since the observation was of the atmosphere, the spectrum is expected to be zero-centered, which is consistent with the result. As discussed in Section 2.2.3, it is important to check what happens to the noise with increasing integration time as seen in Figure 4.7. This is done for the frequency range 250GHz < f < 320 GHz, where the NET values of the still beam a observation closely match the photon-noise model. Frequencies below 250 GHz were excluded due to the unexplained discrepancies, and frequencies above 320 GHz were excluded due to lower atmospheric transmission.

In this frequency range, the spectrum noise is well-centered around zero. Figure 4.7 illustrates how the standard deviation of noise (σ) decreases with different integration times in the range of 1s to 1500s (since we are only using the simulated ”ON” data).

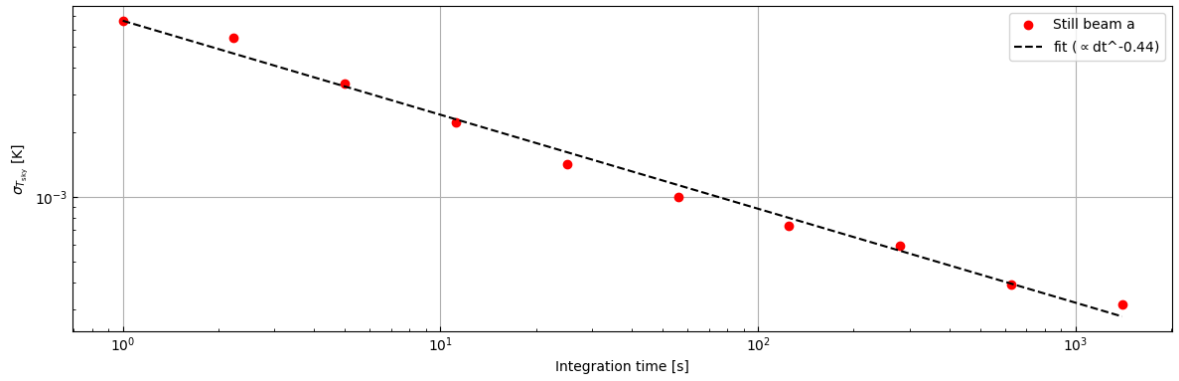

Figure 4.7: Noise as function of integration time for a frequency range of frequency range 250GHz < f < 320 GHz.

The results show that $\sigma \propto \tau^{-0.44}$, which is slightly lower than the expected $\sigma \propto \tau^{-0.5}$ (as discussed in Section 2.2.3). In Section 3.4, NET was defined as the minimum detectable temperature change in the sky for an integration time of 1 second. From Figure 4.7, we can extract σ from the fitted line at an integration time of 1s and compared that to the NET we found earlier to see if they agree.

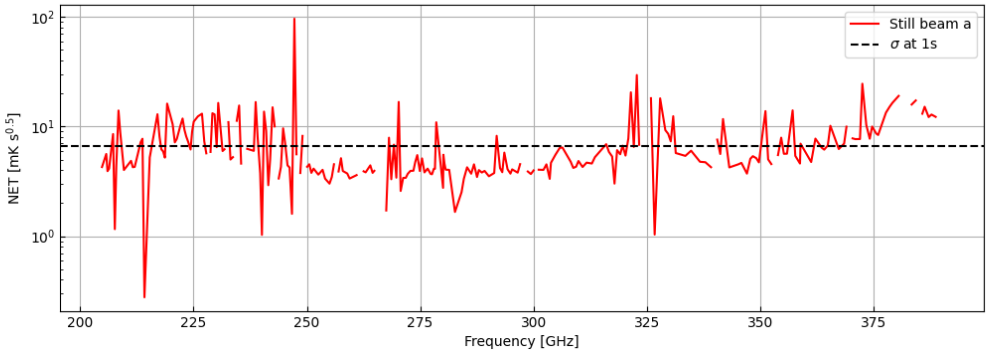

Figure 4.8: The NET of a still beam a observation (red) with σ at an integration of 1s (black).

Figure 4.8 shows that the NET obtained by interpolating σ at 1 second closely matches the NET derived from the PSD of each channel, further validating the results.

4.3. Atmosphere: Still beam ab

After confirming photon-noise-limited sensitivity in the still beam a observation, we looked at an atmosphere observation where both beam a and beam b where used (still beam ab). Note that the telescope is still stationary, but the chopper wheel is activated to alternate between the two beams.

4.3.1. NET

As with the still beam a observation, the NET for the still beam ab observation is derived from the PSD of each channel. A key difference here is that the data is split into beam a and beam b. Figure 4.9 displays the NET for beam a alone, beam b alone, and the combined NET of both beams. For this analysis, only the first 50 minutes of the observation are considered, as detailed in the appendix E, due to anomalies at the end of the observation causing abnormally high temperature readings.

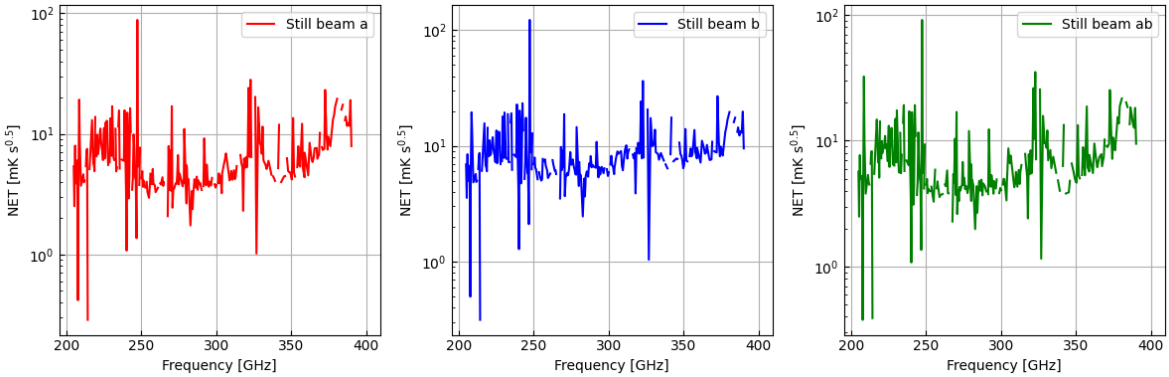

Figure 4.9: NET for each individual channel of a still beam ab observation, where the red plot is only looking at beam a, the blue plot only looking at beam b and the green plot looking at both beam a and b.

When compared to the photon-noise model (Figure 4.10), the NET results show overall agreement, though discrepancies are again evident at frequencies below 250 GHz. Interestingly, beam a exhibits closer alignment with the photon-noise model than beam b. A possible and highly likely explanation for this is the tilt of the chopper wheel, as discussed in Section 2.1.1. This is further supported by an analysis of the PSD for individual channels in beam b, which revealed unexpected patterns (see appendix E). Despite these irregularities, the combined NET for both beams agrees well with the photon-noise model, supporting the validity of the observation.

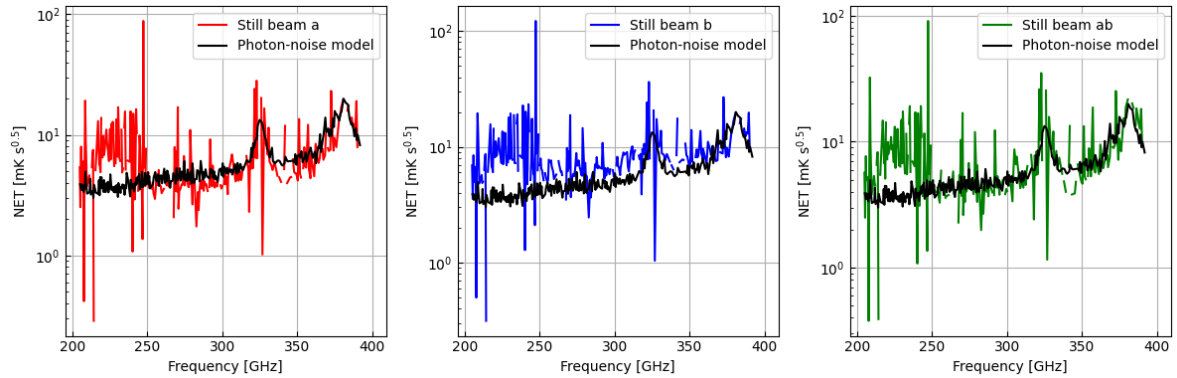

Figure 4.10: NET for each individual channel of a still beam ab observation compared to the photon-noise model (black), where the red plot is only looking at beam a, the blue plot only looking at beam b and the green plot looking at both beam a and b.

4.3.2. Noise in Spectrum

As with the still beam a observation, the spectrum of the still beam ab observation is examined to assess how noise changes with increasing integration time. This analysis uses the ABBA chopping method described in Section 2.3.1, which isolates noise from the signal by processing individual cycles. The averaged spectrum across all cycles is shown in Figure 4.11. Only the first 24 ABBA cycles are included in this analysis, even though 26 cycles were recorded. This is done for the same reasons as mentioned in the NET analyses since there seemed to be unusually high temperatures towards the end of the observation.

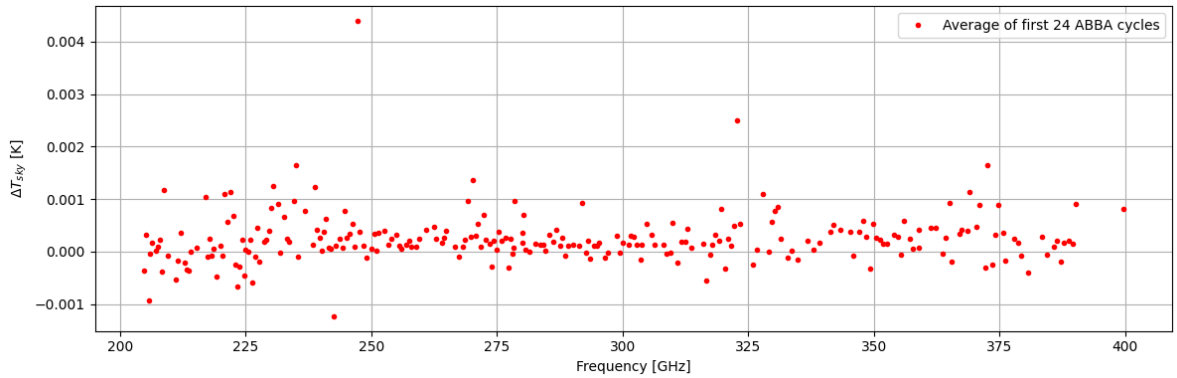

Figure 4.11: Noise in spectrum after performing ABBA chopping averaged over the first 24 ABBA cycles.

For each ABBA cycle, the standard deviation (σ) of the noise was calculated and plotted, as shown in Figure 4.12(a). This time, cycles 25 and 26 are included to further illustrate these aforementioned extremes. To provide additional clarity, the standard deviations are presented in a histogram (Figure 4.12(b). This visualisation highlights that all cycles, except for cycle 25 (indexed as 24), maintain a σ below 0.005 K. Consequently it is decided to exclude cycle 25 from the analysis, but to still include cycle 26.

To evaluate noise reduction with increasing integration time, σ was computed progressively by averaging over an increasing number of cycles. Specifically, the standard deviation was first calculated for cycle 1, then for the average of cycles 1 and 2, and so on, until all cycles were included. This analysis focused on the frequency range of 250 GHz to 300 GHz, as Figure 4.11 indicates minimal fluctuations in this range. The resulting plot of σ against integration time is shown in Figure 4.13.

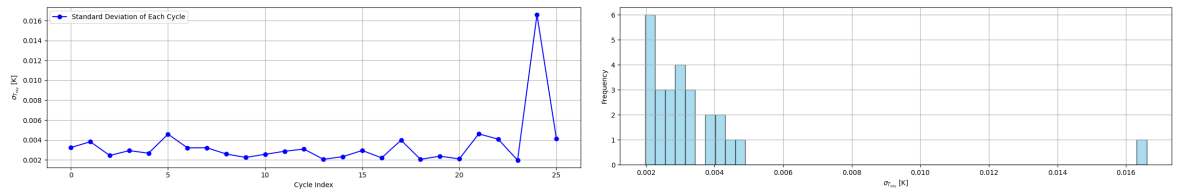

(a) (b)

Figure 4.12: Two plots showing the standard deviation for each individual ABBA cycle. (a) Standard deviation of the noise of each individual ABBA cycle, showing an unusual high value for cycle 25 (indexed as 24). (b) Histogram of the standard deviations of the noise.

The results reveal that σ decreases with increasing integration time, following a relationship of $\sigma \propto \tau^{-0.71}$. This slope is steeper than the expected trend of $\sigma \propto \tau^{-0.5}$.

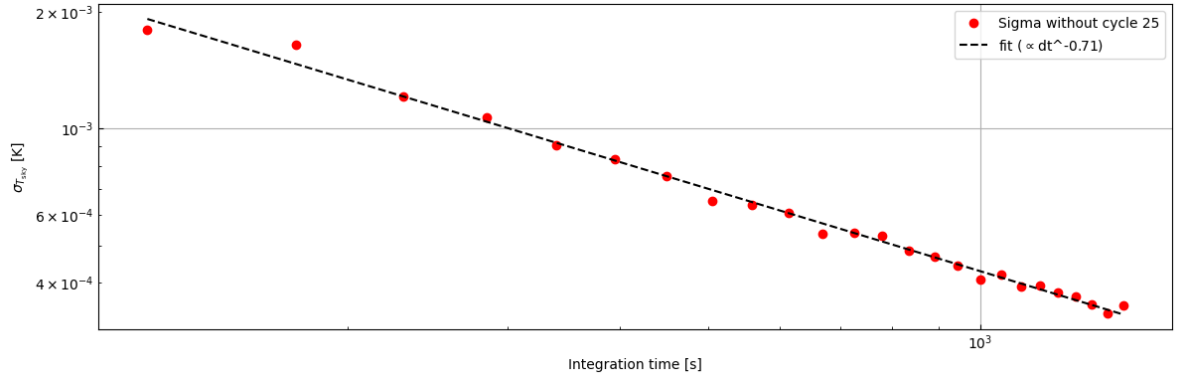

Figure 4.13: Noise as function of integration time for a frequency range of frequency range 250GHz < f < 300 GHz.

There could be many reasons for this, including something as simple as the stability of the atmosphere improving over time. Given that the observation spanned a lengthy period (almost an hour), it can likely be influenced by external factors such as changing atmospheric conditions.

4.4. Mars

4.4.1. Comparison of Observed and Modeled Mars Spectrum

After confirming that the atmosphere observations are photon-noise limited (to a degree), we used these sensitivity insights to assess the telescope's performance with a known astronomical source. Mars was chosen due to its brightness in the submillimetre wavelength range. Two back-to-back observations were used to verify consistency, as shown in Figure 4.14. Here, "psw 1" refers to the first observation, and "psw 2" refers to the second observation. "psw" stands for position switching, where the telescope alternates between two positions on the sky to be able to the perform ABBA chopping, as described in Section 2.3.1.

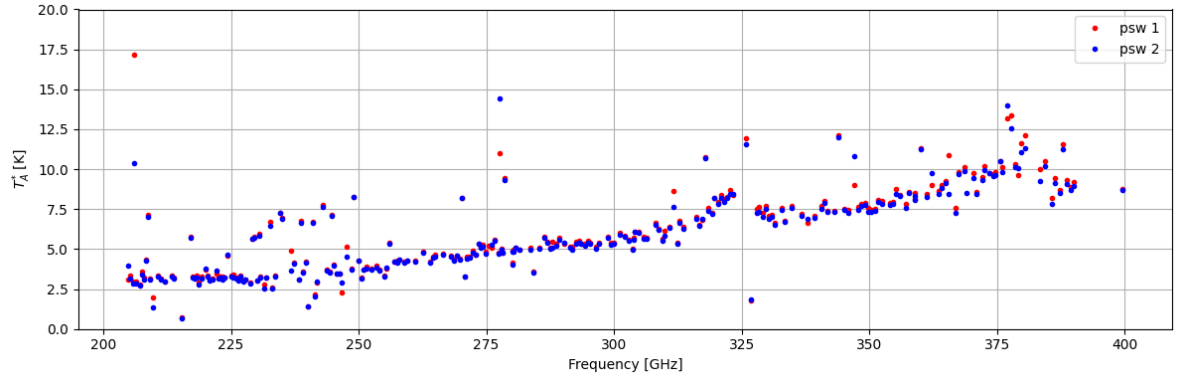

Figure 4.14: Spectrum of two different positions switching (psw) mars observations.

It is important to note that the ABBA chopping method used in this Mars observation differs slightly from the one discussed in Section 2.3.1, which is specific to atmospheric observations, here an ABBA chopping code from Arend Moerman is used [17]. In the Mars observation, averaging is done over the entire segment before performing the subtraction, which can yield different results compared to the atmospheric ABBA method. However, this difference is less pronounced when observing a very bright source like Mars and will only significantly affect the analysis of fainter signals.

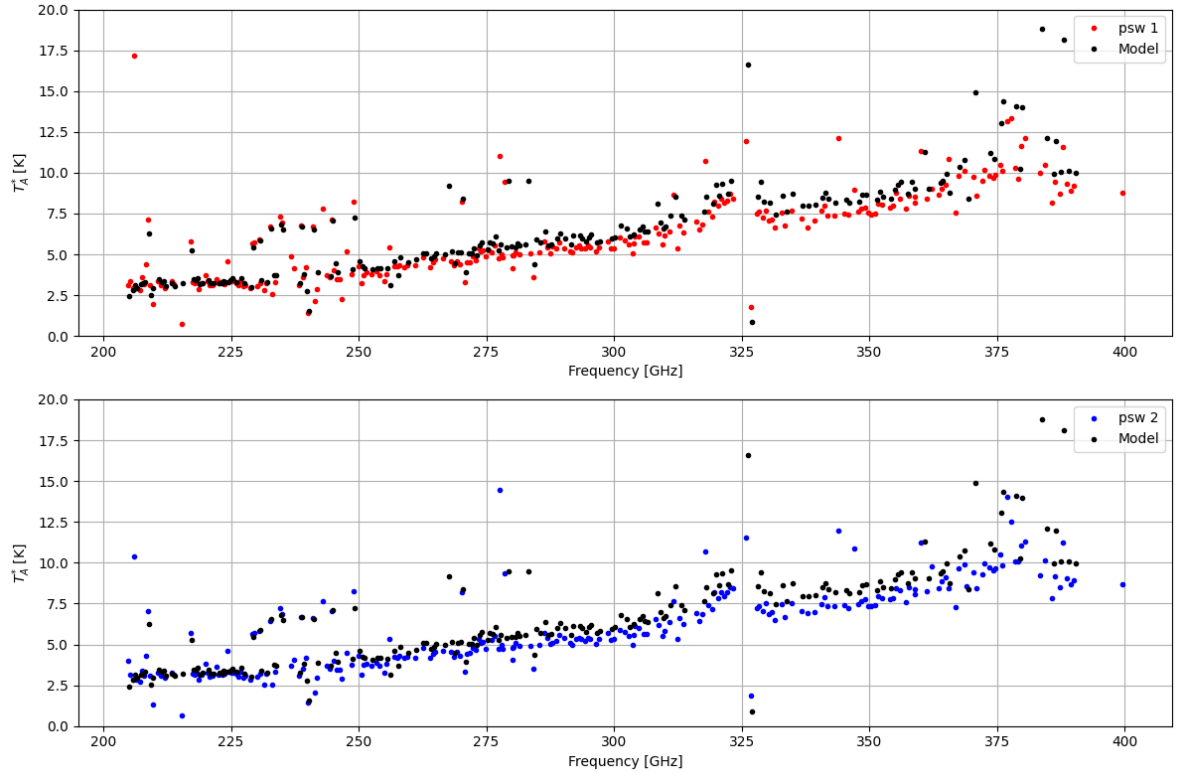

Figure 4.15: Spectrum of two different positions switching (psw) mars observations compared to a known brightness model of Mars.

In Section 3.6, a spectrum of Mars was modeled based on literature values. This modelled spectrum is compared to the observed spectrum, as illustrated in Figure 4.15. Both ”psw 1” and ”psw 2” observations show good agreement with the model, confirming the telescope’s performance for this bright source.

4.4.2. Noise with Increasing Integration Time

To further confirm the spectral sensitivity and calibration of DESHIMA 2.0, we analysed how the noise behaves as the integration time increases. Before performing this analysis, we ensured that the spectrum was centered around zero by subtracting a linear fit from the spectrum. This subtraction removes the signal and leaves only the noise. This procedure was applied to both ”psw 1” and ”psw 2” observations, as shown in Figure 4.16.

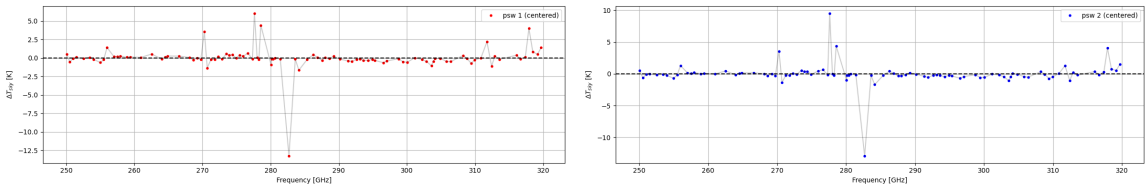

(a) **(b)**

Figure 4.16: Noise in then spectrum of a Mars observation after removing the signal (a) for psw 1 and (b) for psw 2.

Next, the standard deviation of the noise (σ) was calculated for increasing integration times. This was done for the the frequency range of 290GHz - 320GHz. These results are shown in Figure 4.17.

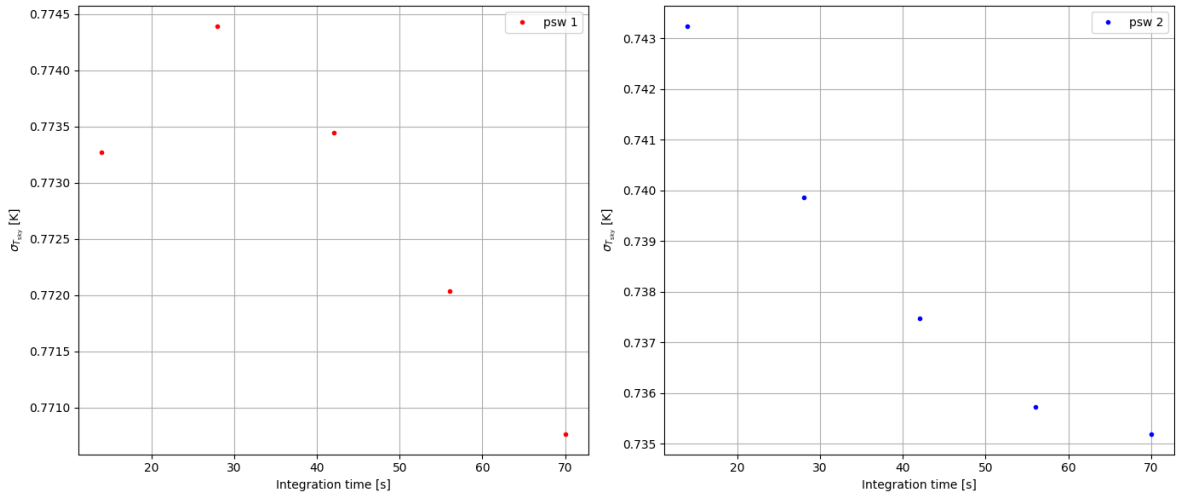

Figure 4.17: Noise as function of integration time for a frequency range of frequency range 290GHz < f < 320 GHz. The left plot (red) is the noise for psw 1 and the right plot (blue) is the noise for psw 2.

Notably, the sigma values for Mars are much larger than those observed in the atmosphere measurements and also don’t improve with integration time. This suggests the presence of a calibration issue. The σ in the Mars spectrum is dominated by systematic errors in calibration (such as issues with KID response [2]), rather than random photon noise. Since Mars is very bright, any systematic error is proportionally amplified, leading to higher measured noise levels.

5

Conclusion

This study assessed the sensitivity and noise limitations of the DESHIMA 2.0 instrument on the ASTE telescope, confirming that it performs within photon-noise limits under specific observational conditions. However, the results also highlight areas that require further refinement.

The still beam a observations demonstrate photon-noise-limited sensitivity, with the NET derived from the observation agreeing well with the photon-noise model. The analysis of spectral noise standard deviation (σ) as a function of integration time follows the expected relationship of $\sigma \propto \tau^{-0.5}$, though a slightly shallower slope of $\sigma \propto \tau^{-0.44}$ was observed, likely due to systematic uncertainties. Channel-to-channel comparisons further support this conclusion, reinforcing the reliability of the telescope for atmospheric observations.

In the still beam ab observations, the NET values for the combined beams (excluding the final two minutes due to anomalies) also align well with the photon-noise model. However, beam b exhibits a slight offset from the expected photon-noise behavior, possibly due to the tilt of the chopper wheel (as discussed in Section 2.1.1) or calibration errors. The ABBA chopping method successfully filters out the noise and shows that the noise reduces with longer integration times as shown in the σ plot. Nevertheless, these results highlight the need to refine the ABBA chopping technique further, ensuring more consistent performance and better handling of systematic errors in beam b.

Mars observations with DESHIMA 2.0 demonstrate good agreement with literature-based models, confirming the instrument's calibration and sensitivity for bright sources. However, the noise behavior in the Mars spectrum deviates from expectations, with higher σ values than those observed in atmospheric measurements. This discrepancy is likely due to systematic errors, including imperfect calibration or limitations in the ABBA chopping method. These errors prevent the expected decrease in σ with integration time, indicating the dominance of systematic errors over random photon noise. While such errors do not significantly affect observations of bright sources like Mars, they limit the telescope's ability to detect weaker signals. Addressing these calibration issues is crucial for extending the instrument's sensitivity to fainter sources.

Overall, the findings indicate that DESHIMA 2.0 is photon-noise-limited for atmospheric observations. However, the results also highlight systematic issues when observing astronomical sources. The discussed ABBA chopping method in this paper needs to be refined to be applicable not only for atmospheric observations but also for astronomical sources. Addressing these calibration and systematic issues, especially in the ABBA chopping technique, is crucial for improving the telescope's performance and extending its sensitivity to both bright and faint astronomical sources.

5.1. Recommondations and Future Prospects

To improve the performance of the DESHIMA 2.0 instrument, several recommendations are made for future work. First, the ABBA chopping technique, while effective for atmospheric observations, requires further refinement to be applicable for astronomical sources. Specifically, it should be adapted to bet-

ter handle systematic errors and ensure consistent performance when observing both bright and faint sources. This could involve modifications to the chopping analysis, as well as improved calibration techniques that can mitigate the offset observed in beam b and better account for instrumental imperfections.

Further investigation is also needed to resolve the systematic errors identified, particularly in the Mars observations. Addressing issues like calibration inaccuracies and limitations in the ABBA chopping analysis could help reduce noise and improve telescope sensitivity. Extending these analyses to fainter astronomical sources would validate the instrument's sensitivity and provide insights for detecting weaker signals. Finally, exploring alternative noise analysis methods, such as Allan variance, may yield more accurate assessments of noise behavior over long integration times. These efforts would refine DESHIMA 2.0's overall performance and broaden its capabilities for a wider range of astronomical observations.

Acknowledgements

I would like to begin by expressing my heartfelt gratitude to my supervisor, Akira Endo, for his unwavering support and guidance throughout my thesis journey. His enthusiasm for the project and his constant availability, even on his ”papa days,” meant so much to me and truly helped me grow as a young researcher. He provided me with invaluable insights, encouraged me to exchange ideas with others, and gave me the opportunity to experience what it means to be part of a research group.

I am especially grateful to him for the unforgettable experience of traveling to Chile, where I could see the telescope in action and witness how theory connects to practice. This trip not only deepened my understanding but also showed me that research is far more than sitting at a desk—it is a dynamic and collaborative journey. His encouragement pushed me to deliver my best work, allowing me to complete a project I am genuinely proud of.

I also want to thank Kenichi Karatsu and Arend Moerman for providing the necessary data for my models. A special thanks to Arend Moerman for patiently helping me understand his code and walking me through its details. My appreciation extends to the entire DESHIMA group for their feedback during meetings and for making me feel like a valued member of the team. I would also like to thank Sander Otte for taking the time out of his busy schedule to form the thesis committee, an effort I truly appreciate.

Finally, I want to thank my friends for their companionship during study sessions, their encouragement during tough times, and their willingness to listen to my endless stories about my project—even if they didn’t fully understand them! Their shared experiences and advice were incredibly valuable in helping me navigate challenges and stay motivated.

Thank you all for making this journey an enriching and unforgettable experience.

Bibliography

[1] A. Taniguchi et al. “DESHIMA 2.0: development of an integrated superconducting spectrometer for science-grade astronomical observations”. In: *Journal of Low Temperature Physics* 209 (2022), pp. 278–286. DOI: 10.1007/s10909-022-02888-5.

[2] T. Takekoshi et al. “DESHIMA on ASTE: On□Sky Responsivity Calibration of the Integrated Superconducting Spectrometer”. In: *Journal of Low Temperature Physics* (2020), pp. 231–239. DOI: 10.1007/s10909-020-02338-0.

[3] ALMA. *Atmosphere model*. URL: https://almascience.eso.org/about-alma/atmosphere-model.

[4] J. Baselmans. “Kinetic Inductance Detectors”. In: *Journal of Low Temperature Physics* 167 (2012), pp. 292–304. DOI: 10.1007/s10909-011-0448-8.

[5] Asantha Cooray Caitlin M. Casey Desika Narayanan. “Dusty star-forming galaxies at high redshift”. In: *Physics Reports* 541 (2014), pp. 45–161. DOI: 10.1016/j.physrep.2014.02.009.

[6] A. D’Amico and P. Mazzetti. *Noise in Physical Systems and 1/f Noise - 1985*. Proceedings of the 8th International Conference on Noise in Physical Systems and the 4th International Conference on 1/f Noise, Rome, September 9-13, 1985. Amsterdam: North-Holland, 1986. ISBN: 9780444869920.

[7] A. Endo and R. Rajan. “Course presentation for EE3350TU Introduction to Radio Astronomy”. In: *TU Delft* ().

[8] A. Endo and A. Taniguchi. *desim*. 2024. URL: https://github.com/deshima-dev/desim.

[9] A. Endo, P. d. Visser, and J. Baselmans. “EE4635 Superconducting Astronomical Instrumentation L1-L10”. In: *TU Delft* (2020).

[10] A. Endo et al. “First light demonstration of the integrated superconducting spectrometer”. In: *Nature Astronomy* 3.10 (2019), pp. 989–996. DOI: 10.1038/s41550-019-0850-8.

[11] M.J. Gouwerok. “A Gas Emission Setup to Evaluate Wideband Sub-mm Spectrometers”. In: *Master Thesis [Delft University of Technology]* (2021). URL: https://repository.tudelft.nl/record/uuid:d3381216-dc06-4ebf-aa2f-617be8875427.

[12] E. Huijten. “TiEMPO:Time-Dependent End-to-End Model for Post-process Optimization of the DESHIMA Spectrometer”. In: *Bachelor’s Thesis [Delft University of Technology]* (2020). URL: http://resolver.tudelft.nl/uuid:5302e10e-3b56-4d4d-a1fd-6a1d58f57abd..

[13] ITU. *Handbook on Radio Astronomy*. Third Edition. https://www.itu.int/dms$_{pub/itu-r/opb/hdb/R-HDB-22-2013-PDF-E.pdf}$. Place des Nations, CH-1211 Geneva 20, Switzerland: RADIOCOMMUNICATION BUREAU, 2013.

[14] E Lellouch. *Mars Thermal Emission Model*. Model developed for calculating the thermal emission of Mars between 1990 and 2020 across frequencies of 30-5000 GHz. Includes atmospheric and surface/subsurface radiative transfer equations. 2008. URL: https://lesia.obspm.fr/perso/emmanuel-lellouch/mars/index.php.

[15] A. S. Long. “Taming Giants: Studies on the Growth, Regulation, and Evolution of Dusty, Star-Forming Galaxies in the Early Universe”. In: *UNIVERSITY OF CALIFORNIA, IRVINE Dissertation* (2022). Dissertation for DOCTOR OF PHILOSOPHY, p. 162. URL: https://escholarship.org/uc/item/3pm505s1.

[16] A. Moerman. “Aperture efficiency analysis - data from 13-18 July 2024”. In: (2024). URL: https://deshima.kibe.la/@arendmoerman/8269.

[17] A. Moerman. *Data reduction pipeline for DESHIMA 2.0 data of the 2024 campaign*. 2024. URL: https://github.com/arendMoerman/d24_tools.

[18] A. Moerman. “PyPO analysis of tilted chopper blade”. In: (2024). URL: https://deshima.kibe.la/@arendmoerman/83549.

[19] Committee on Radio Astronomy Frequencies. *Sensitivity of radio astronomy systems (theoretical considerations)*. 2023. URL: https://www.craf.eu/useful-equations/sensitivity-of-radio-astronomy-systems-theoretical-considerations/ (visited on 12/24/2020).

[20] Y. Roelvink. “Simulation of a High-Redshift Line-Emitting Galaxy Detection with DESHIMA using TiEMPO”. In: *Bachelor’s Thesis [Delft University of Technology]* (2020). URL: http://resolver.%20tudelft.nl/uuid:c878c9d5-f9af-44fd-83c4-a4bd8a7496b5..

[21] APEX Observatory Ayllu de Sequitor. *Atacama Pathfinder Experiment (APEX)*. 2024. URL: https://almascience.eso.org/about-alma/atmosphere-model.

[22] Y. Sukul. “Principal component analysis on atmospheric noise measured with an integrated superconducting spectrometer”. In: *Bachelor’s Thesis [Delft University of Technology]* (2019). URL: https://repository.tudelft.nl/record/uuid:a75fde14-e7fb-401c-9c47-2f954fc5e70c.

[23] J. Tiebosch. “Photon-bunching in groundbased submillimeter-wave astronomy”. In: *Bachelor’s Thesis [Delft University of Technology]* (2022). URL: https://repository.tudelft.nl/record/uuid:7d150ea8-1cdd-4584-a99e-65392599bfb9.

[24] K. Volk. “Chopping and Nodding for Mid-Infrared Astronomy”. In: (2007). URL: http://www.gemini.edu/sciops/%20instruments/mir/chopnod.pdf.

[25] S. X. Wang et al. “An ALMA Survey of Submillimeter Galaxies in the Extended Chandra Deep Field-South: The AGN Fraction and X-Ray Properties of Submillimeter Galaxies”. In: *The Astrophysical Journal* 778 (2013). Published by The American Astronomical Society, p. 179. DOI: 10.1088/0004-637X/778/2/179.

[26] Peter D. Welch. “The Use of Fast Fourier Transform for the Estimation of Power Spectra: A Method Based on Time Averaging Over Short, Modified Periodograms”. In: *IEEE Transactions on Audio and Electroacoustics* AU-15.2 (1967), pp. 70–73. DOI: 10.1109/TAU.1967.1161901.

A

ABBA Chopping Code

Below is the python code used to create the ABBA chopping algorithm

```
"""
#Loading python packages
import decode as dc
from decode import load, plot, select
import pickle
import numpy as np
import xarray as xr
import pandas as pd
import matplotlib.pyplot as plt
from IPython.display import Image
from scipy import signal
from pathlib import Path
import deshima_sensitivity as dsm

xr.set_options(keep_attrs=True)
from d24_tools import tools as d24tools
from d24_tools import atmosphere as atm
from d24_tools import methods

#Loading Data
obsid = "20241001200932"

path_of_dems_file = "/Users/madelief/Desktop/BEP/Observations data/2 Oct Still Beam/dems_" + obsid + ".zarr.zip"
da = dc.qlook.load_dems(path_of_dems_file) # Load data to xarray DataArraysa
da_scan = dc.select.by(da, "state", ["SCAN"]) # Select by state label "SCAN"

#Splitting data up in chops
# Generating indices for beam A and beam B based on the beam type
idx_A = np.squeeze(np.argwhere(da.beam.data == "A"))
idx_B = np.squeeze(np.argwhere(da.beam.data == "B"))

# Ensure the indices cover all data
all_idx = np.arange(da_sub.shape[0])
assert all_idx.size == (idx_A.size + idx_B.size)

# Chunk consecutive indices within A and B observations
chunk_list_A = methods._consecutive(idx_A)
chunk_list_B = methods._consecutive(idx_B)

# Check the structure of chunk lists to confirm small chunks
print("Number of A chunks:", len(chunk_list_A))
print("Number of B chunks:", len(chunk_list_B))
print("First few A chunks (lengths):", [len(chunk) for chunk in chunk_list_A[:20]])
print("First few B chunks (lengths):", [len(chunk) for chunk in chunk_list_B[:20]])

# Initialize lists to store mean values for each despiked chunk
```

```
mean_values_A = []
mean_values_B = []

# Despike and calculate mean for each chunk in beam A
for idx_chunk_A in chunk_list_A:
    if idx_chunk_A.size >= 3:  # Only despike if the chunk has at least 3 values
        # Despike by removing the first and last values
        despiked_chunk_A = idx_chunk_A[1:-1]

        # Calculate the mean across all frequencies for the despiked chunk
        mean_A_chunk = np.mean(Tsky[despiked_chunk_A, :], axis=0)
        mean_values_A.append(mean_A_chunk)

# Despike and calculate mean for each chunk in beam B
for idx_chunk_B in chunk_list_B:
    if idx_chunk_B.size >= 3:  # Only despike if the chunk has at least 3 values
        # Despike by removing the first and last values
        despiked_chunk_B = idx_chunk_B[1:-1]

        # Calculate the mean across all frequencies for the despiked chunk
        mean_B_chunk = np.mean(Tsky[despiked_chunk_B, :], axis=0)
        mean_values_B.append(mean_B_chunk)

# Converting lists to arrays for easier handling
mean_values_A = np.array(mean_values_A)
mean_values_B = np.array(mean_values_B)

# Final diagnostics to confirm the shape of the results
print("Shape of mean_values_A:", mean_values_A.shape)  # Expecting (num_chunks_A, 301)
print("Shape of mean_values_B:", mean_values_B.shape)  # Expecting (num_chunks_B, 301)


#Finding the mean of each ABBA cycle

def ABBA_chop(mean_values_A, mean_values_B, num_segments=104, chunks_per_segment=300):

    num_channels = mean_values_A.shape[1]  # Number of channels (columns) in the data

    # Create arrays to store the mean for each cycle and each segment
    cycles = num_segments // 4  # 26 cycles in total
    cycle_means = np.zeros((cycles, num_channels))  # Array for cycle means
    segment_means_all = np.zeros((num_segments, num_channels))  # Array for individual
        segment means

    # Loop through each cycle
    for cycle_idx in range(cycles):
        segment_means = np.zeros((4, num_channels))  # Create array to store segment means
            within each cycle

        for segment_in_cycle in range(4):
            # Compute segment index in the overall sequence of segments
            segment_idx = cycle_idx * 4 + segment_in_cycle

            # Determine the starting and ending chunk indices for this segment
            start_chunk = segment_idx * chunks_per_segment
            end_chunk = start_chunk + chunks_per_segment

            # Compute the element-wise difference between A and B for each chunk in the
                segment
            if segment_in_cycle in [0, 3]:  # Segments 1 and 4 in the cycle: A-B
                segment_difference = mean_values_A[start_chunk:end_chunk, :] - mean_values_B[
                    start_chunk:end_chunk, :]
            else:  # Segments 2 and 3 in the cycle: B-A
                segment_difference = mean_values_B[start_chunk:end_chunk, :] - mean_values_A[
                    start_chunk:end_chunk, :]

            # Compute the mean of the differences for this segment
            segment_mean_difference = np.nanmean(segment_difference, axis=0)

            # Store the mean difference for this segment
            segment_means[segment_in_cycle, :] = segment_mean_difference
```

```
            segment_means_all[segment_idx, :] = segment_mean_difference  # Store in full
                segment array

        # Mean value across the 4 segments in the cycle
        cycle_means[cycle_idx, :] = np.nanmean(segment_means, axis=0)

    return cycle_means, segment_means_all

# Call the function and capture both outputs
cycle_avg, segment_avg = ABBA_chop(mean_values_A, mean_values_B, num_segments=104,
    chunks_per_segment=300)
```

B

Parameters used in Deshima-sensitivity for photon-noise model

Below are the input parameters of DESHIMA sensitivity used to calculate the photon-noise model. The parameters marked with (*) are the parameters that are discussed in the report.

```
spectrometer_sensitivity parameters:
    F = F*
    pwv = 1.0*
    EL = 60*
    R = Q*
    eta_M1_spill = 0.99
    eta_M2_spill = 0.90
    eta_wo_spill = 0.99
    n_wo_mirrors = 4.0
    window_AR  = True
    eta_co = 0.65
    eta_lens_antenna_rad = 0.81
    eta_circuit = eta*
    eta_IBF = 0.5
    KID_excess_noise_factor = 1.1
    theta_maj = 22.0 np.pi / 180.0 / 60.0 / 60.0
    theta_min = 22.0 np.pi / 180.0 / 60.0 / 60.0
    eta_mb = 0.6
    telescope_diameter = 10.0
    Tb_cmb = 2.725
    Tp_amb = 273.0
    Tp_cabin = 290.0
    Tp_co = 4.0
    Tp_chip = 0.12
    snr = 5.0
    obs_hourst = 10.0
    on_source_fraction = 0.4 * 0.9
    on_off = False*
```

The output of deshima-sensitivity actually gives the NEFD (instead of the NET), but using the following equations, the NET can be calculated. The first equation is from the deshima-sensitivity code to find the NEFD. The NET can be calculated using the second equation. By combining these two equations,

we can derive the last equation, which shows that the main beam efficiency (η_{mb}) and the aperture efficiency (η_A) cancel out. This shows that these efficiencies do not directly affect the calculation of the NET, and so are not relevant to the calculation of NET.

$$NEFD = NEP_{kid} \times \frac{R}{F} \times \frac{1}{\sqrt{2}_{Hz\leftrightarrow s} A_g} \times \frac{\eta_{IBF} 2_{pol}}{\eta_{inst}\eta_{atm}\eta_a\eta_{for}} \tag{B.1}$$

$$NET_{sky} = NEFD \frac{\eta_{atm}\eta_a A_g}{2_{pol} k_B} \tag{B.2}$$

$$NET_{sky} = \frac{NEP_{kid}}{\sqrt{2}_{Hz\leftrightarrow s}} \frac{\eta_{IBF}}{\eta_{ins}\eta_{for}} \frac{R}{F} \tag{B.3}$$

C

Parameters Mars Model

To create a model of the Mars spectrum, a brightness model was developed using the following input parameters:

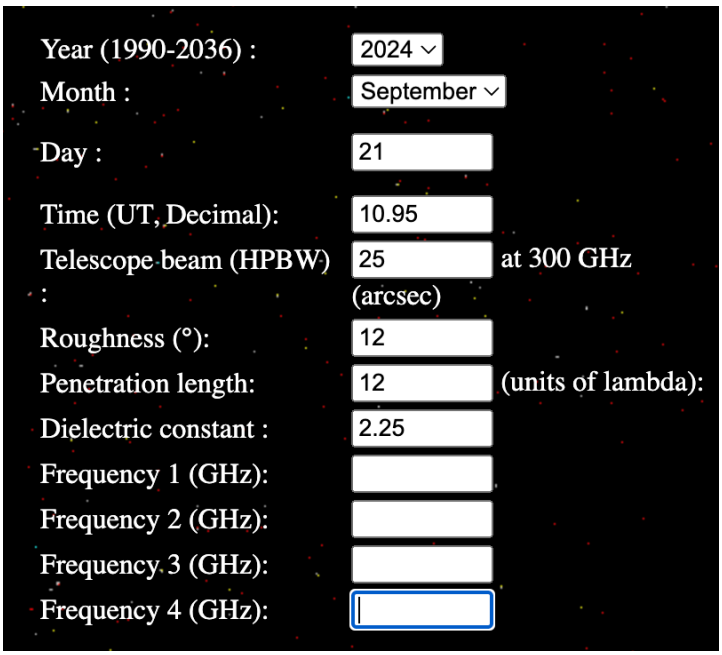

Figure C.1: Parameters used in Mars brightness model

Roughness(referring to the average slope of the Mars surface) and penetration length (indicating the depth of the surface layer contributing to the brightness temperature) are intrinsic characteristics of Mars. Upon investigation, it was found that the values used for these parameters were relatively standard defaults, which were also applied in this brightness model. Frequencies were defined within the range of 200 GHz to 400 GHz, with intervals of 10 GHz. The date and time of the observations correspond to the specific moment when Mars was observed.

D

Still beam A observation - PSD in 230GHz - 250GHz range

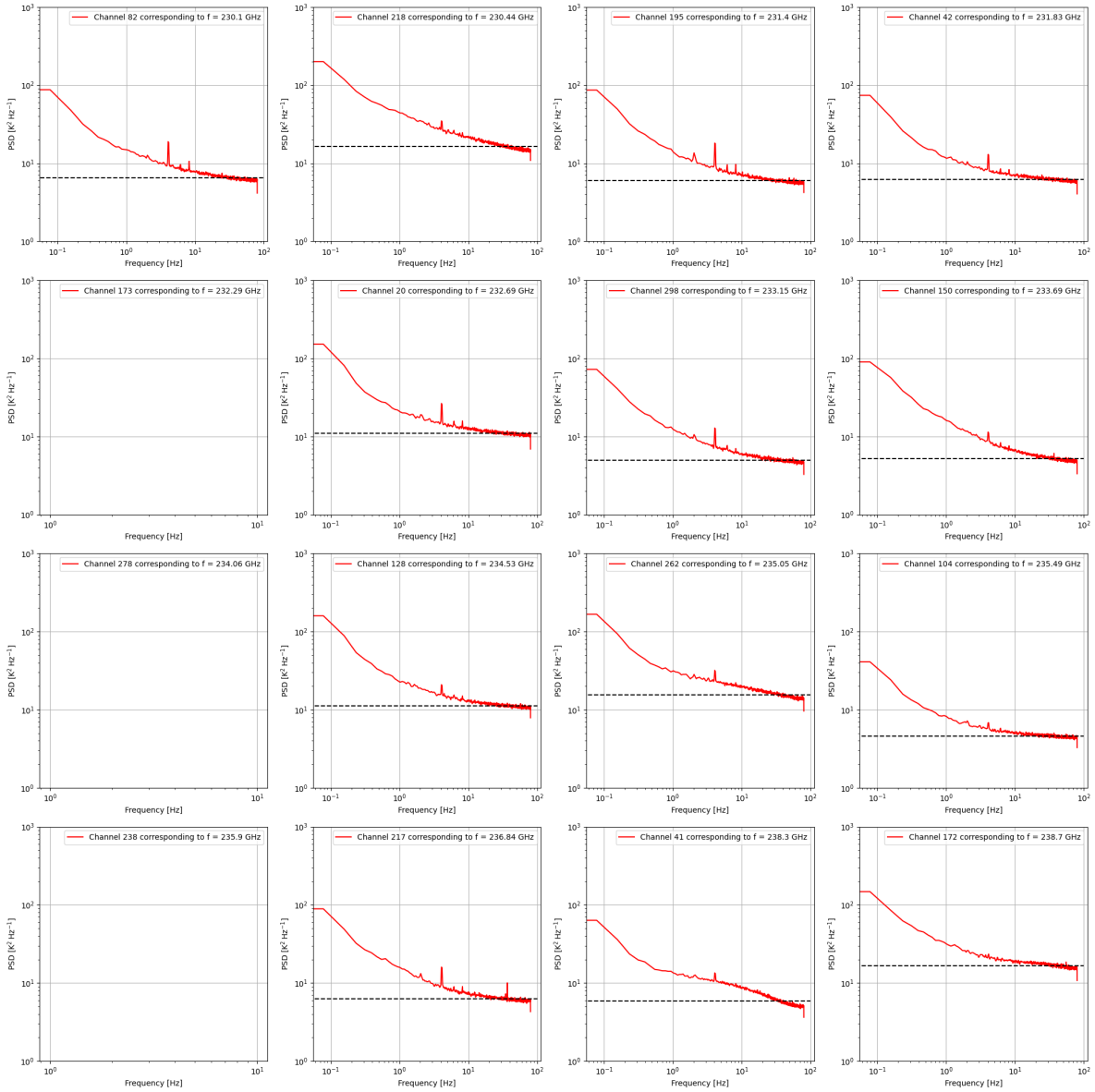

Figure D.1: PSD plots for channels in range 225GHz to 250GHz for the Still Beam a observation. The Black lines are the variances after 10Hz, they represent the NET values

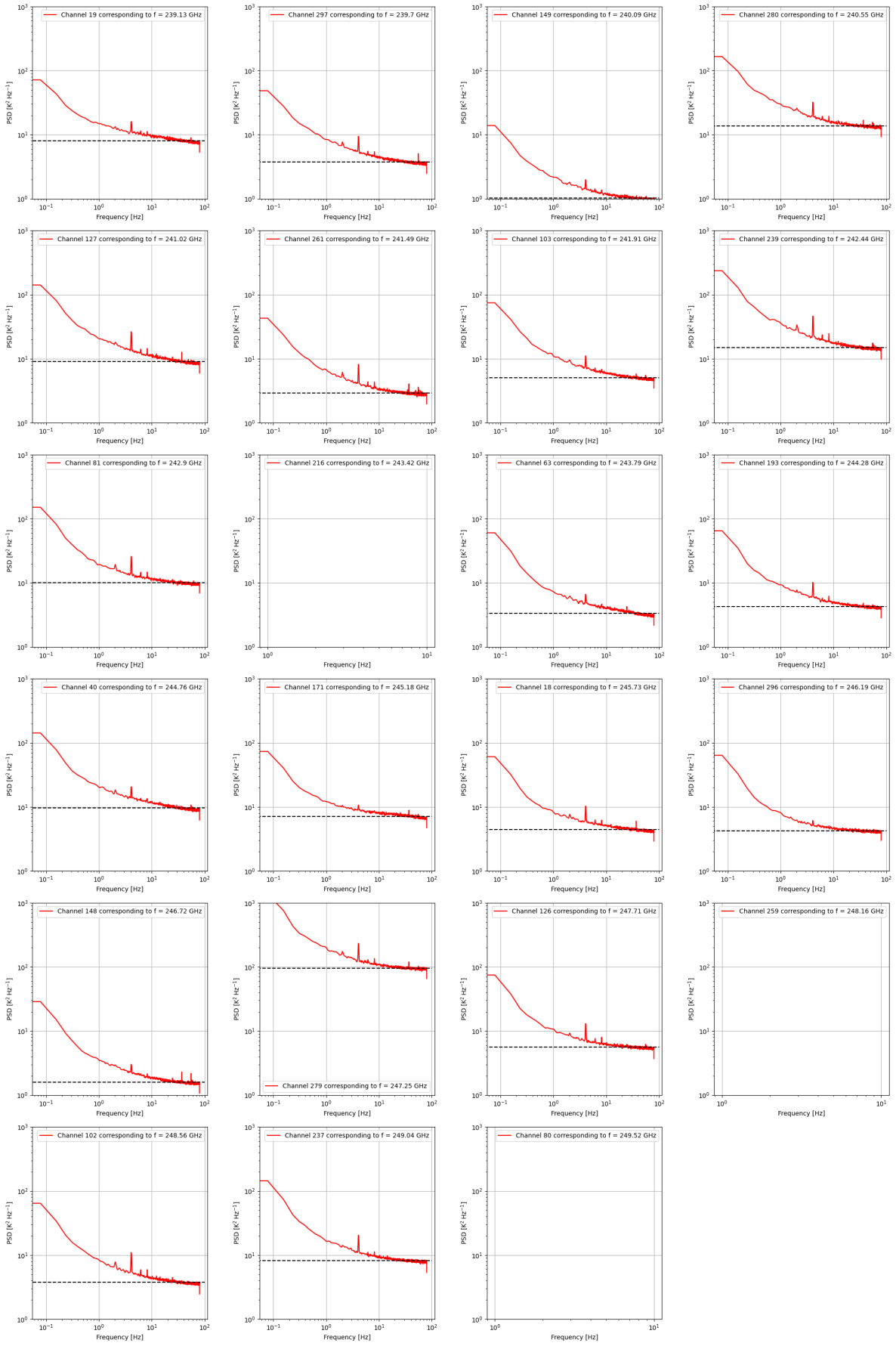

Figure D.2: PSD plots for channels in range 225GHz to 250GHz for the Still Beam a observation. The Black lines are the variances after 10Hz, they represent the NET values

E

Still beam AB Observation

E.1. Limiting observation to 50 minutes

Only the first 50 minutes of the still beam ab observation are analysed in this report. This is because there seem to be unusually high temperatures towards the end of the observation. Looking at the time domain of the observation we can see that for beam a these are abnormally high.

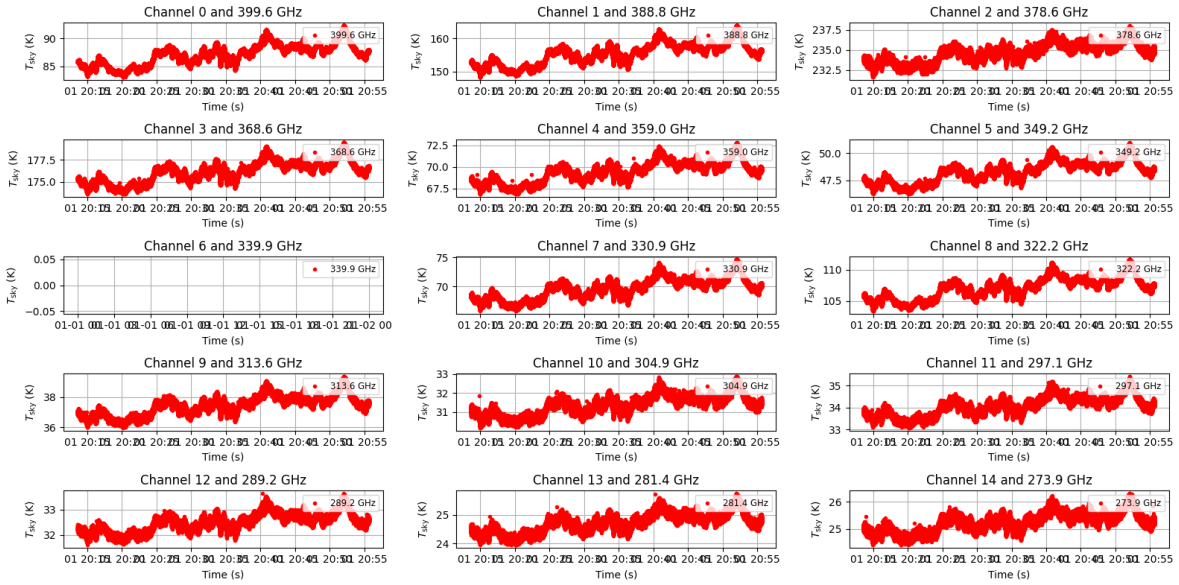

Figure E.1: Time domain for the first 14 channels of beam a

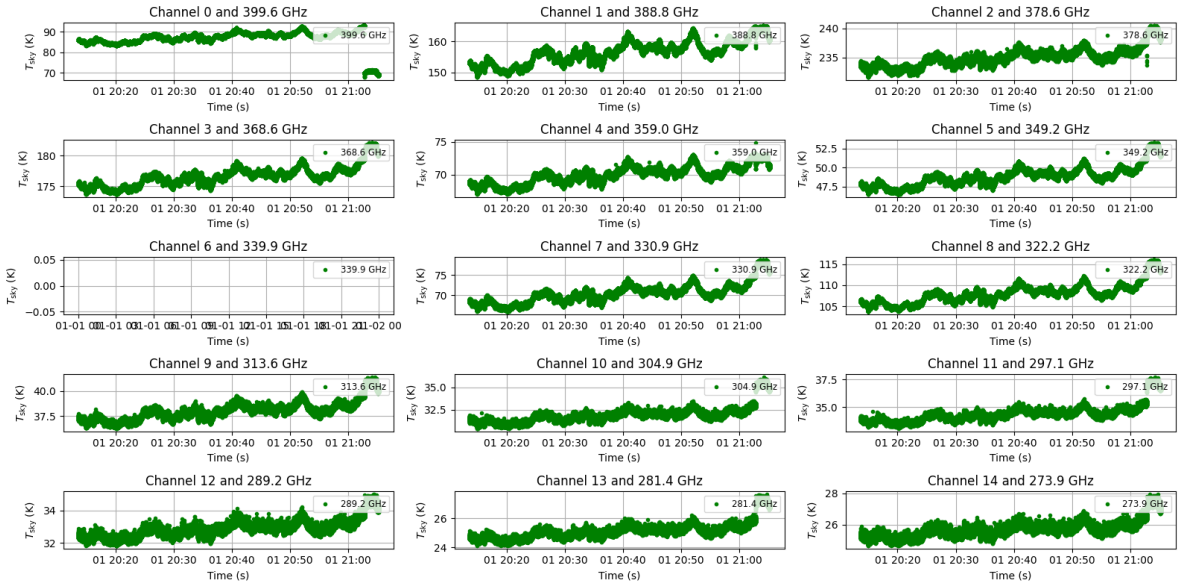

Figure E.2: Time domain for the first 14 channels of beam b

E.2. PSD for beam a and beam b for frequency range

PSD for both beam a and beam b in the still beam ab observation show some unexpected peaks in the beam b. It is unclear where this is coming from, but could explain the offset in the NET values.

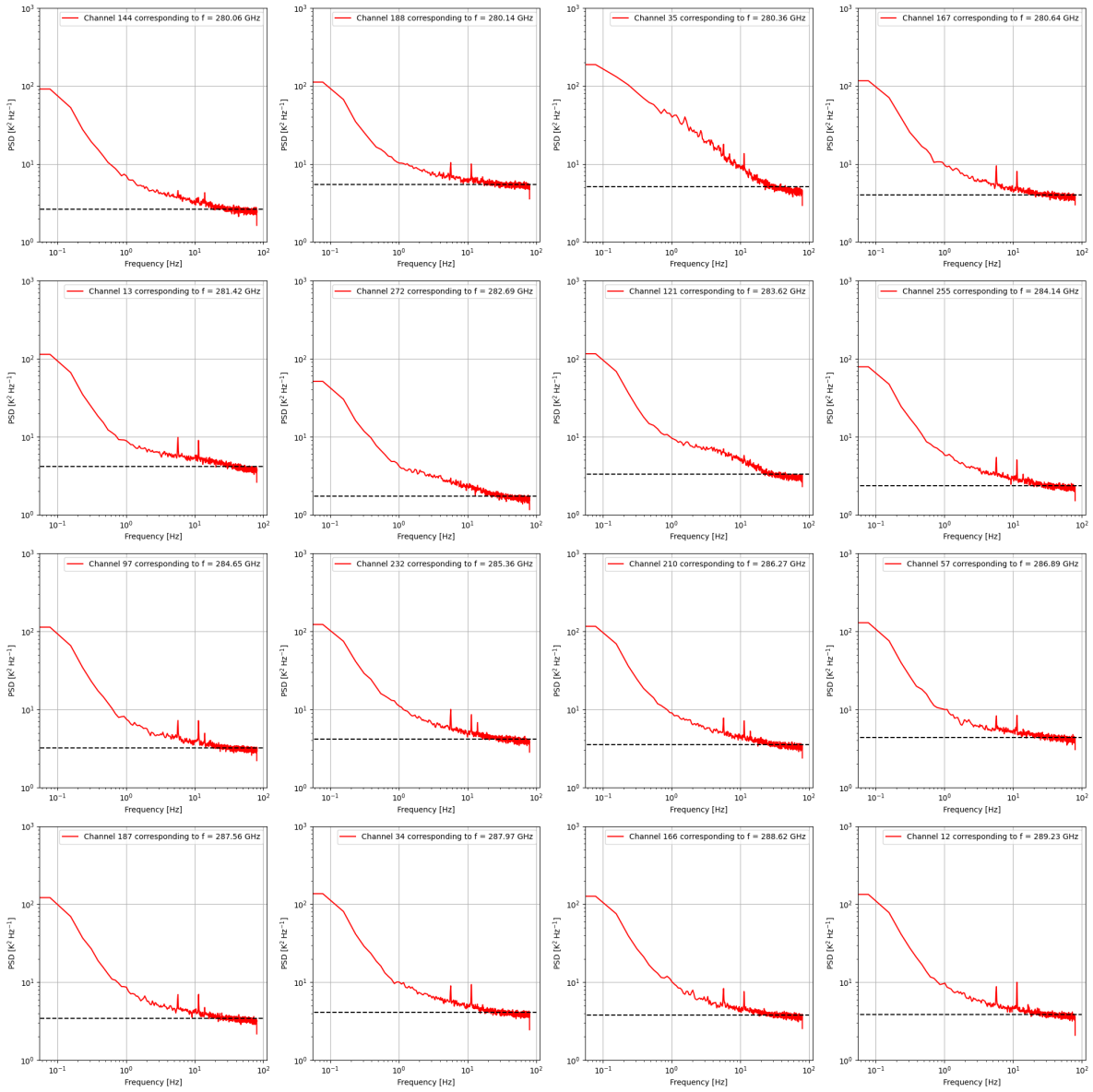

Figure E.3: PSD for beam a in still beam ab observation for frequency range 280GHz to 290GHz

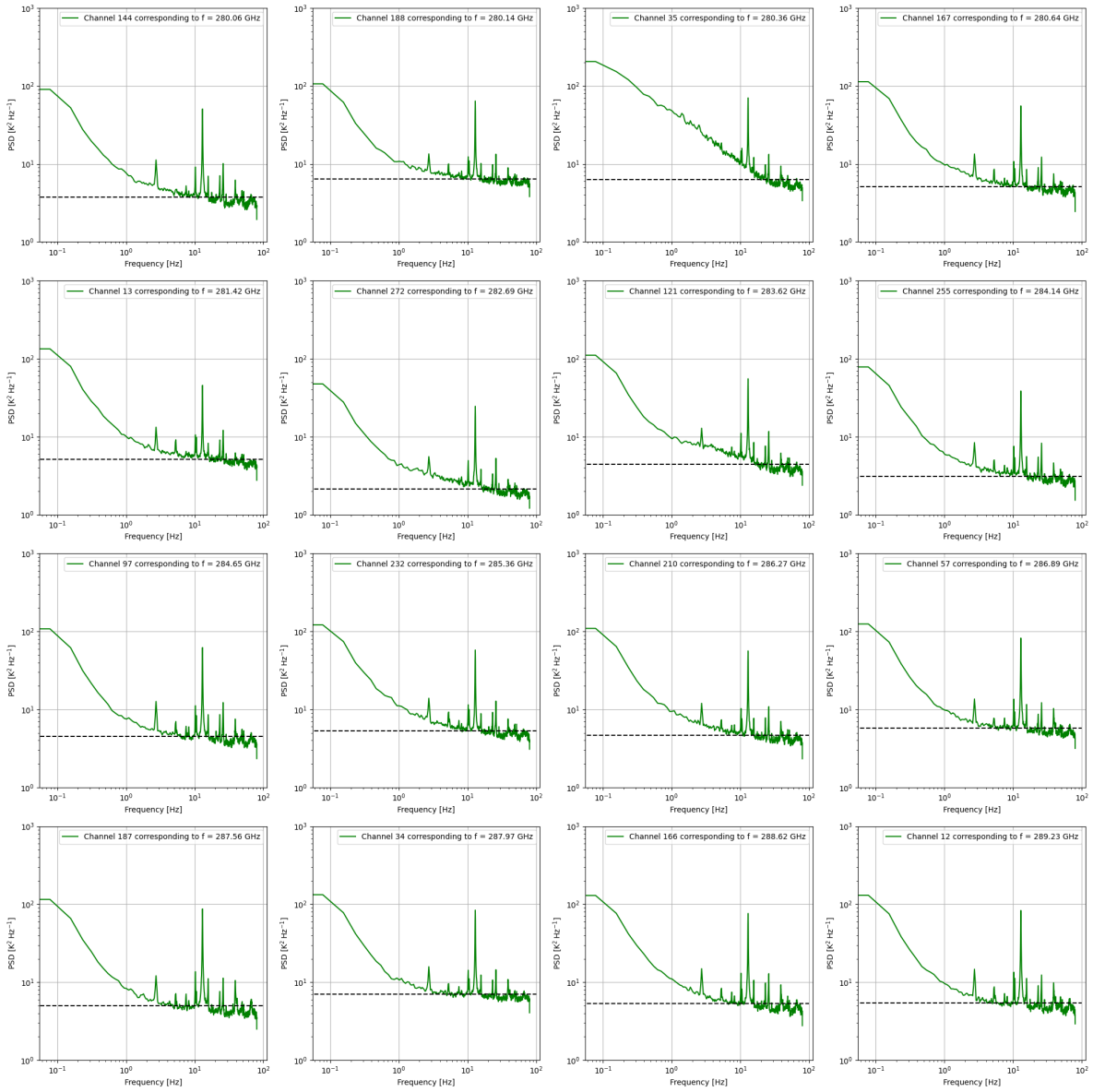

Figure E.4: PSD for beam b in still beam ab observation for frequency range 280GHz to 290GHz

E.3. Noise in each individual ABBA cycle

Noise in each individual ABBA cycle. Note how cycle 25 shows unexpected values.

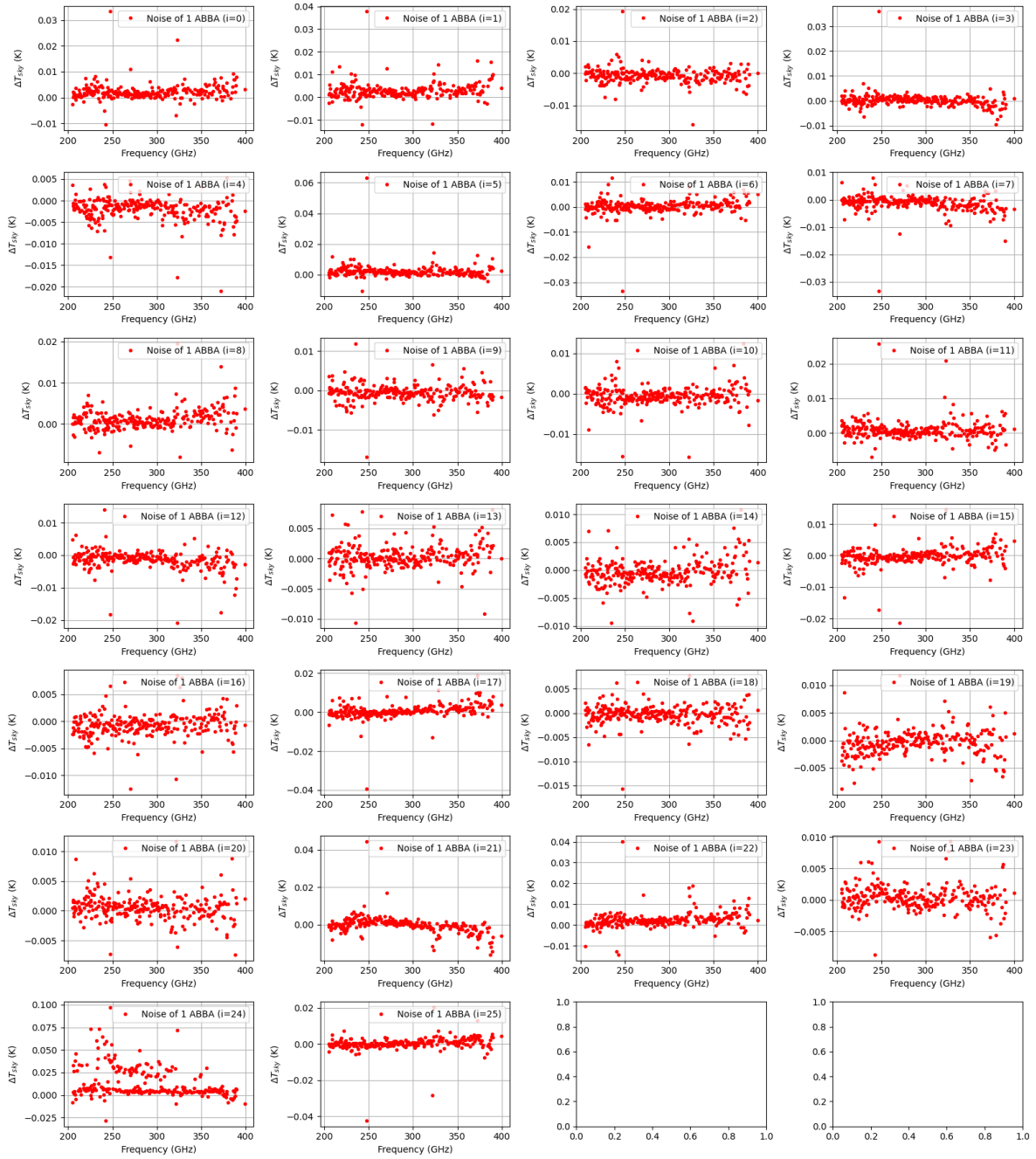

Figure E.5: Time domain for the first 14 channels of beam a